Supplementary Information for

Effect of Metal Substitution on the Intrinsic Activity of Iridium-Based Oxides for the Oxygen Evolution Reaction

Yinghao Xu,‡ [a] Yi-Hsuan Wu,‡ [a] Paula M. Abdala,[a] Connor Sherwin,[b] Veronica Celorrio,[b] Diana Piankova,[a] Payal Chaudhary,[c] Vitaly Alexandrov,[c],[d] Agnieszka Kierzkowska,[a] Denis A. Kuznetsov,*[a] and Christoph R. Müller*[a]

[a] Y. Xu, Dr. Y.-H. Wu, Dr. P. M. Abdala, Dr. D. Piankova, Dr. A. Kierzkowska, Dr. D. A. Kuznetsov, Prof. Dr. C. R. Müller
ETH Zürich, Department of Mechanical and Process Engineering, 8092 Zürich, Switzerland
E-mail: denisk@ethz.ch; muelchri@ethz.ch

[b] Dr. C. Sherwin, Dr. V. Celorrio
Diamond Light Source, Harwell Science and Innovation Campus, Didcot, OX11 0DE, United Kingdom

[c] P. Chaudhary, Prof. Dr. V. Alexandrov
Department of Chemical and Biomolecular Engineering, University of Nebraska-Lincoln, Lincoln, Nebraska 68588, United States

[d] Prof. Dr. V. Alexandrov
Nebraska Center for Materials and Nanoscience, University of Nebraska-Lincoln, Lincoln, Nebraska 68588, United States

[‡] These authors contributed equally to this work

Experimental Section

Chemicals

Iridium(IV) chloride hydrate (Strem), chromium(III) acetylacetonate (99.99%, Sigma-Aldrich), molybdenum(VI) dioxide bis(acetylacetonate) (97%, Sigma-Aldrich), tungsten(VI) chloride (>99.9%, Thermo Fisher Scientific), indium(III) acetylacetonate (≥99.99%, Sigma-Aldrich), oleylamine (>98%, Sigma-Aldrich), sodium oleate (≥82%, Sigma-Aldrich), 1-octadecene (90%, Sigma-Aldrich), n-hexane (≥95%, Avantor), chloroform (99.8%, Thermo Fisher Scientific), ethanol (100%, Alcosuisse AG) were used as purchased without any further purification.

Colloidal Synthesis of Ir-M nanoparticles

To synthesize the Ir-M nanoparticles a colloidal synthesis approach was utilized using a modified literature recipe.[1] In a typical experiment, 0.1 mmol (or 0.05 mmol for Ir-poor sample, *i.e.*, composition of Ir < 50 at%) of the iridium precursor ($IrCl_4 \cdot xH_2O$) and the precursor for the second metal (M = Cr, Mo, W, In) with the desired molar ratio were dissolved in 3 mL oleylamine (this mixture is referred to as "Ir-M mixture" below). Next, the Ir-M mixture was sonicated followed by heating at *ca.* 80 °C in a sand bath until the complete dissolution of the solid precursors was achieved. Next, sodium oleate (200 mg) was dissolved in 2 mL 1-octadecene and 1 mL oleylamine in a separate 50-mL three-neck flask under constant N_2 flow while stirring at 450 rpm. Subsequently, the solution was heated to 160 °C (10 °C · min^{-1} ramp rate) to obtain a homogeneous solution. During the heating step, a drop in temperature (for 2~3 °C) was observed when passing *ca.* 125 °C, probably due to the endothermic gel formation.

Next, the as-prepared Ir-M mixture was slowly injected into a three-neck flask. Once the gel was fully dissolved (the temperature should be increased by *ca.* 5 °C if there is a gel residue), the stirring rate was adjusted to 300 rpm. For degassing and dehydration, the flask was evacuated by vacuum pumping (< 0.25 mbar) for 5 min followed by purging with nitrogen for 2 min. The evacuation-N_2 purging step was repeated twice, followed by a heating up of the mixture to 300 °C (10 °C·min^{-1}) and left stirring in a N_2 atmosphere for 2 h. Upon completion of the reaction, the mixture was cooled down to 70 °C.

For removal of the capping ligands, *ca.* 2 mL hexane and an excess amount of ethanol (*ca.* 60 ml) were added to the mixture. The product was separated by centrifugation (8500 rpm, 4.5 min) and washed with ethanol (30 ml each time); the procedure was repeated 3-5 times. The final product was dispersed in chloroform or hexane (*ca.* 10–15 ml). The concentration of the Ir-M colloids was measured by inductively coupled plasma-optical emission spectrometry (ICP-OES) (see **Table S1**). The colloidal solution was stored in a fridge (*ca.* 4 °C) in a sealed vial.

Electrochemical Characterization

The electrochemical tests were performed using a three-electrode single-compartment cell. The catalyst ink (1 ml mixture) contained 200 μg Ir-M colloids (the exact volume of the added colloid solution was based on the concentration determined by ICP-OES) and 40 μg carbon black (in tetrahydrofuran) which were dispersed in a total of 990 μL of the solvent (tetrahydrofuran) and 10 μL of Nafion. Next, 10 μL of the catalyst ink was drop casted onto the working electrode yielding 2 $\mu g_{catalyst}$ (or 10 $\mu g_{catalyst}$ cm^{-2}) on the rotating-disk, glassy carbon electrode (0.196 cm^2, Pine Research). The electrodes were dried at ambient condition for at least 12 h prior to the measurements. The reference electrode was Ag/AgCl (saturated KCl) when using $HClO_4$ as the electrolyte or Hg/HgO (1 M KOH) when using KOH as the electrolyte. A Pt wire or graphite rod was used as the counter electrode. The experiments were conducted in O_2-saturated 0.1 M $HClO_4$ (or 0.1 M KOH, 99.99% KOH).

The reference electrode was calibrated using the same electrolyte as in the electrocatalystic performance assessment (*i.e.*, 0.1 M $HClO_4$ or 0.1 M KOH) saturated with H_2 by measuring the voltage corresponding to zero current (as an open circuit voltage or from cyclic voltammetry (CV) scan at 5 mV s^{-1}) for hydrogen oxidation/evolution using a platinum disk electrode. The relationships between the reversible hydrogen electrode and the reference electrodes are:

$$V_{RHE} = V_{Ag/AgCl} + 0.235\ V \quad (0.1\ M\ HClO_4)$$

$$V_{RHE} = V_{Hg/HgO} + 0.860\ V \quad (0.1\ M\ KOH).$$

The Ohmic resistance was determined in the high-frequency region (100 kHz ~ 1 kHz) of the electrochemical impedance spectroscopy (EIS) measurements. Resistances of ~ 23 Ω (0.1 M $HClO_4$) ~and 46 Ω (0.1 M KOH) were applied for the iR correction.

For the catalyst activation step (*i.e.*, to convert the metallic phase(s) into IrO_x:M) cyclic voltammetry applying a scan rate of 10 mV s^{-1} within the potential window of 0.85 $V_{Ag/AgCl}$ and 1.40 $V_{Ag/AgCl}$ (1.085 V_{RHE}~1.635 V_{RHE}) was used; the rotation rate was set to 1600 rpm. Overall, the Ir-M catalysts showed an increasing current over the first 8~10 CVs in 0.1 M $HClO_4$, except $Ir_{30}In_{70}$ for which a clear decrease of the current during continuous cycling was observed. The 10^{th} CV was reported for activity comparison in this work. At least seven electrodes were measured for each catalyst/condition to provide accurate statistics for each batch of Ir-M nanoparticles. The electrocatalytic stability tests were performed using chronoamperometry measurements at 1.55 V_{RHE} (rotation rate 1000 rpm).

The electrochemically active surface area (ECSA) was estimated by double layer capacitance measurements. To this end, the working electrode was prepared without the addition of carbon black (using the same material loading of 2 $\mu g_{catalyst}$) and cycled in a potential window ±50 mV

around the open-circuit potential in O_2-saturated 0.1 M $HClO_4$. The following scan rates were used: 5, 10, 20, 50, 100, 150, 200 mV s^{-1} with (10 s rest between each cycle). The ECSA was measured before and after the catalyst activation cycles (10 CV cycles as described above) to probe the difference in the ECSA between the pristine and the oxidized Ir-M nanoparticles. The capacitance current at each scan rate at the forward (anodic) and backward (cathodic) scan was averaged. The specific double layer capacitance of the iridium oxide surface was selected as 1.18 mF cm^{-2}.[2] (Although we acknowledge that the specific capacitance provided in the literature was estimated in 0.5 M H_2SO_4, the selection of the absolute value would not impact the trends discussed in the work.)

The OER turnover frequency (TOF, unit: s^{-1}) was estimated using the following formula:

$$TOF = \frac{I}{z\,F\,n}$$

where I is the current (unit: A) measured at a specific potential under OER conditions, z is the number of charges transferred to form one O_2 molecule (*i.e.*, z = 4). F is the Faradaic constant (i.e. 96485.3 C/mol-e^-) and n is the number of catalytically active sites (unit: mol). Here, we assume a Faradaic efficiency of 100 % towards OER. For instance, for 2 µg of the monometallic Ir precursor, n = 1×10^{-8} mol.

We used three different approaches to define n, resulting in turn in three different estimates of the TOF.

TOF based on a TEM-based estimation of the surface area

$$\boldsymbol{TOF_{surface}} = \frac{I}{z\,F\,n_{surface}}$$

$$n_{surface} = \frac{\frac{total\ TEM-based\ surface\ area\ of\ the\ catalyst}{unit\ area\ per\ single\ Ir\ atom}}{6.023 \times 10^{23}}$$

Here, $n_{surface}$ represent the number of Ir sites at the surface of the nanoparticles. The total surface area of the catalysts per electrode (*i.e.*, the average surface area of the nanoparticle scaled by the average number of nanoparticles loaded on the electrode) was derived from transmission electron microscopy (TEM) images assuming a perfect spherical shape of the nanoparticles, *i.e.*, $S = 4\pi r^2$ where r is the average radius of the Ir-M nanoparticles. The average number of particles (N_{av}) loaded onto a single electrode was calculated using the density of iridium (22.56 g/cm^3).

$N_{av} = V_{total}/V_1$

$V_{total} = m/\rho$ (m is the mass of Ir loaded onto a single electrode; ρ is the density of iridium)

$V_1 = 4/3\ \pi r^3$ (r is the mean radius of the Ir-M nanoparticles as assessed by TEM)

The unit area per Ir atom of the (010) crystallographic facet is (3.838 × 3.838 Å^2) / 2 = 7.365 × 10^{-16} cm^2 for metallic Ir (½ is used because there are two Ir atoms located within a (010) facet).

Based on this estimation, $TOF_{surface}$ is generally seen as an upper boundary of the TOF as the number of active sites is underestimated.

TOF based on the total Ir loading

$$\boldsymbol{TOF_{bulk}} = \frac{I}{z\ F\ n_{total}}$$

$$n_{total} = \frac{mass\ of\ the\ loaded\ catalysts\ (g) \times mass\ fraction\ of\ Ir\ in\ Ir\text{-}M}{molar\ mass\ of\ Ir\ (192.217\ g\ mol^{-1})}$$

where n_{total} is the total number of Ir atoms loaded onto the electrode.

While $TOF_{surface}$ represents an upper bound for the TOF, TOF_{bulk} provides a lower bound.

TOF based on the total IrO_x content

TOF_{EA} is derived from TOF_{bulk} only considering the fraction of metallic iridium that is converted into IrO_x (γ, which is estimated from linear combination fitting analysis of the Ir L_3-edge XAS data) is catalytically active, *i.e.*,

$$\boldsymbol{TOF_{EA}} = TOF_{bulk}/\gamma$$

Online electrochemistry-mass spectroscopy (EC-MS)

Electrochemistry-mass spectrometry (EC-MS) measurements were performed using an EC-MS system from SpectroInlets in which a PTFE electrochemical cell is positioned on top of a semipermeable silicon membrane chip (SpectroInlets) to allow gas products to diffuse through the chip into the MS chamber enabling a real-time detection of desorbed products and their quantitative analysis.[3] Here, 0.1 M $HClO_4$ was used as the electrolyte, a Pt wire as the counter electrode and Ag/AgCl (saturated KCl, Pine Research) as the reference electrode. A gold disk (5 mm diameter) was used as the working electrode. The catalyst ink, composed of a Ir-M : carbon black ratio of 5 : 1 (w/w) was drop cast onto the gold disk to yield a loading of 10 $\mu g_{catalyst}$. Potentials were controlled by a Biologic SP-300 potentiostat. The working electrode was

connected through a 100 Ω resistor to stabilize the potential. Potentials indicated for the measurements performed in the EC-MS cell are reported without correction for ohmic losses.

^{18}O-labelled 0.1 M $HClO_4$ was prepared by mixing perchloric acid (70%, Sigma-Aldrich) with H_2O-^{18}O (97% ^{18}O purity, Medical Isotopes, Inc.). To label the catalysts with ^{18}O, the electrodes were cycled 2~3 times from OCV to *ca.* 1.47 V_{RHE} (to reach a current of *ca.* 0.2 mA) in ^{18}O-labelled 0.1 M $HClO_4$. To this end, the electrodes were held at a series of incrementally increased constant currents (2 μA, 5 μA, 10 μA, 25 μA, and 50 μA for 5 min at each current). Afterwards, the electrode, the membrane and the cell were thoroughly rinsed with deionized water and dried with a flow of compressed air. Next, the electrodes containing ^{18}O-labelled catalysts were cycled in $HClO_4$-^{16}O (10 CV cycles in the potential range 1.2 to 1.47 V_{RHE}; the upper voltage was selected as a value to reach the current ~ 0.2 mA (*i.e., ca.* 1.47 V_{RHE}). Subsequently, the electrodes were held at a series of constant currents (5 μA, 10 μA, 20 μA, 50 μA, 100 μA; followed by 100 μA, 50 μA, 20 μA, 10 μA, 5 μA for 2 min at each step). These data were used for an internal calibration of the MS detector.

Ex Situ **Characterization**

X-ray diffraction patterns were acquired using a PANalytical Empyrean X-ray powder diffractometer using Cu Kα radiation (λ =1.5418 Å, 40 mA, and 40 kV). Samples were measured in the 2θ range of 15–95° using a step size of 0.05º with a time duration of 320 s per step.

Inductively coupled plasma optical emission spectrometry (ICP-OES) measurements were performed using an Agilent 5100 VDV instrument.

X-ray photoelectron spectroscopy (XPS) data were acquired using a PHI Quantera SXM (ULVAC-PHI, Chanhassen, MN, USA). A monochromatic Al Kα (1486.6 eV) source with a beam diameter of 200 μm was selected. The analyser operated in constant-analyzer energy (CAE) mode. Survey spectra were acquired with a pass energy of 280 eV, a step time of 20 ms and a step size of 1.0 eV. High-resolution narrow scans were collected using a step size of 0.1 eV (pass energy of 55 eV). The binding energy in the narrowly-scanned spectra were calibrated with the peak of Au $4f_{7/2}$ at 84.0 eV using a gold foil and using the C *1s* peak at 248.8 eV for surface adventitious carbon species (C–C, sp^3).

Transmission electron microscopy (TEM) imaging was performed using a FEI Talos F200X microscope equipped with a high-brightness field-emission gun, a high-angle annular dark field (HAADF) detector, and a large collection-angle EDX detector.

High-resolution high-angular annular field scanning transmission electron microscopy (HAADF-HRTSTEM) imaging, selected area electron diffraction (SAED), and Energy Dispersive X-

ray spectroscopy measurements were performed on a double Cs-corrected JEM-ARM300F Grand ARM "Vortex," operated at 300 kV and equipped with 2 large-area SDD EDX detectors with a 100 mm^2 active area. The specimens were prepared by drop-casting a suspension of nanoparticles onto Cu grids with ultra-thin carbon film. The HRSTEM-HAADF images were denoised using a plugin in the commercial software DigitalMicrograph from Gatan.[4] Integrated intensity electron diffraction profiles were obtained by azimuthally integrating SAED patterns using the software eRDF Analyzer. [5]

***In situ* X-ray Absorption Spectroscopy (XAS)**

The XAS experiments were performed at beamline B18, Diamond Light Source, United Kingdom. The energy of the incident X-ray beam was tuned by a Si (111) channel-cut monochromator, $\lambda/\Delta\lambda \sim 5{,}000$. XAS experiments of the reference samples, *i.e.*, iridium powder (99.9% trace metals basis, Sigma-Aldrich), iridium (III) acetylacetonate ($Ir(acac)_3$) (Biosynth), and IrO_2 (Pulver, 99 %, Alfa Aesar) were performed in transmission mode. It is noted that IrO_2 (Permion) from Alfa Aesar is in a dihydrate form, *i.e.*, it contains iridium hydroxides. For the Ir-M samples XAS measurements were performed in fluorescence mode. The Pt L_3-edge of a Pt foil was utilized as reference for the Ir L_3-edge or W L_3-edge energy calibration (calibrated to 11564 eV) prior to the measurements. An energy shift of 3.3 eV was applied to all Ir L_3-edge spectra.

For each experiment, the Ir-M nanoparticles were dropped onto a piece of carbon paper (*ca.* 2 $mg_{catalyst}$ cm^{-2} without the addition of carbon black). The electrode was mounted into a custom-made three-electrode cell (with Kapton-plate window) available at the beamline B18. The electrolyte was 0.1 M $HClO_4$. The protocol for the *in situ* XAS measurements was as following:

1) XAS spectra were collected for samples immersed in the electrolyte at an open circuit voltage (OCV).
2) The electrodes were cycled between 0.85 $V_{Ag/AgCl}$ and 1.40 $V_{Ag/AgCl}$ (50 CV cycles, scan rate 100 mV s^{-1}).
3) XAS spectra were collected again at OCV (labelled as “OCV cycled” in **Figure 4**).
4) The electrodes were held at a series of constant potentials: 0.9 $V_{Ag/AgCl}$, 1.0 $V_{Ag/AgCl}$, 1.05 $V_{Ag/AgCl}$, 1.10 $V_{Ag/AgCl}$, 1.125 $V_{Ag/AgCl}$, 1.15 $V_{Ag/AgCl}$, 1.175 $V_{Ag/AgCl}$, 1.20 $V_{Ag/AgCl}$, 1.225 $V_{Ag/AgCl}$, 1.25 $V_{Ag/AgCl}$, 1.30 $V_{Ag/AgCl}$.
5) XAS spectra were collected again at OCV.

Each XAS measurement consisted of three scans. Three XAS spectra were collected for each condition and averaged prior to their analysis.

The acquired spectra were extracted, calibrated and normalized using the Athena software[6]:

- The white line (WL) peak positions were determined via the peak fitting function. The continuum edge step was modelled by an arctangent function centered at the absorption edge (inflection point of the rising edge) with a height of unity. One Lorentzian component was employed without constraints in width and E_0 position to represent the average Ir state in each Ir-M catalyst.
- For linear combination fitting (LCF) analysis, each white line was fitted using the following references: Ir powder, $Ir(acac)_3$, and IrO_2, within the range of –20 eV before and +15 eV after the edge.

The extended X-ray absorption fine structure (EXAFS) was fitted using the Artemis software[6]; multiple scattering paths were included in the fittings (see **Table S2**).

Computational details

Density functional theory (DFT) calculations were performed using the Vienna Ab initio Simulation Package (VASP).[7, 8] The projector augmented wave (PAW) potentials (W_pv, Ir, O, H) were employed[9] and exchange-correlation functionals were described using the PBE scheme.[10] A plane-wave cutoff energy of 400 eV and a 3 × 2 × 1 Monkhorst-Pack *k*-point grid was used in all calculations. Smearing was introduced using the first-order Methfessel-Paxton method with a smearing width of 0.2 eV. The truncation criterion for electronic steps was chosen to be 10^{-6} eV and the precision mode was set to accurate.

The rutile $IrO_2(110)$ surfaces were modelled as periodic four-layer slabs with a 3 × 2 surface supercell (9.53 × 12.74 $Å^2$) and a vacuum gap of about 18 Å. The bottom two layers were kept fixed, and all other atoms were relaxed until all forces were less than 0.05 eV $Å^{-1}$. Coordinatively unsaturated (cus) Ir atoms were substituted with W atoms to study the effect of W-doping on OER. The difference in the relaxed lattice parameters of the W-doped and undoped surface supercells was found to be less than 1%. Therefore, the same supercell size was used for all systems and only atomic coordinates were relaxed in the final calculations.

Figures and Tables

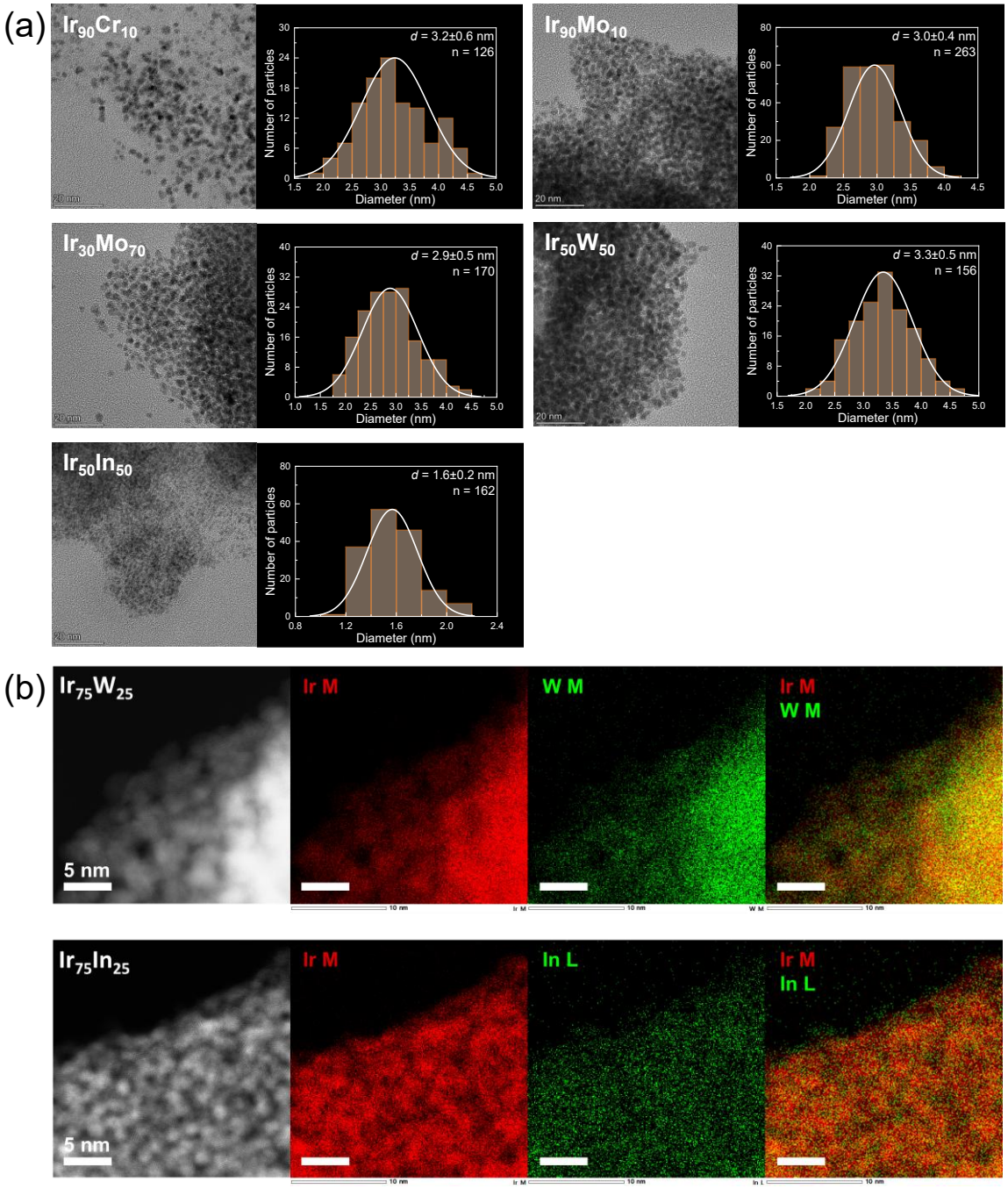

Figure S1. (a) Bright-field TEM images and histograms of the particle size distribution of the as-synthesized Ir and Ir-M (M = Cr, Mo, W, and In) nanoparticles not shown in **Figure 1**. (b) HAADF-STEM images of the selected area of $Ir_{75}W_{25}$ and $Ir_{75}In_{25}$ nanoparticles studied by EDX and the elemental maps of Ir, W, In and their overlap, respectively.

Table S1. Nominal (used for synthesis) and actual ratio determined by ICP-OES analysis between iridium and the second metal M (M = Cr, Mo, W, In) in the bimetallic Ir-M nanoparticles.

Nominal ratio of Ir-M	Actual composition determined by ICP-OES
$Ir_{90}Cr_{10}$	$Ir_{91}Cr_{9}$
$Ir_{65}Cr_{35}$	$Ir_{64}Cr_{36}$
$Ir_{50}Cr_{50}$	$Ir_{49}Cr_{51}$
$Ir_{30}Cr_{70}$	$Ir_{34}Cr_{66}$
$Ir_{90}Mo_{10}$	$Ir_{91}Mo_{9}$
$Ir_{70}Mo_{30}$	$Ir_{68}Mo_{32}$
$Ir_{50}Mo_{50}$	$Ir_{55}Mo_{45}$
$Ir_{30}Mo_{70}$	$Ir_{32}Mo_{68}$
$Ir_{90}W_{10}$	$Ir_{91}W_{9}$
$Ir_{75}W_{25}$	$Ir_{74}W_{26}$
$Ir_{50}W_{50}$	$Ir_{46}W_{54}$
$Ir_{40}W_{60}$	$Ir_{39}W_{61}$
$Ir_{90}In_{10}$	$Ir_{90}In_{10}$
$Ir_{75}In_{25}$	$Ir_{77}In_{23}$
$Ir_{50}In_{50}$	$Ir_{46}In_{54}$
$Ir_{30}In_{70}$	$Ir_{30}In_{70}$

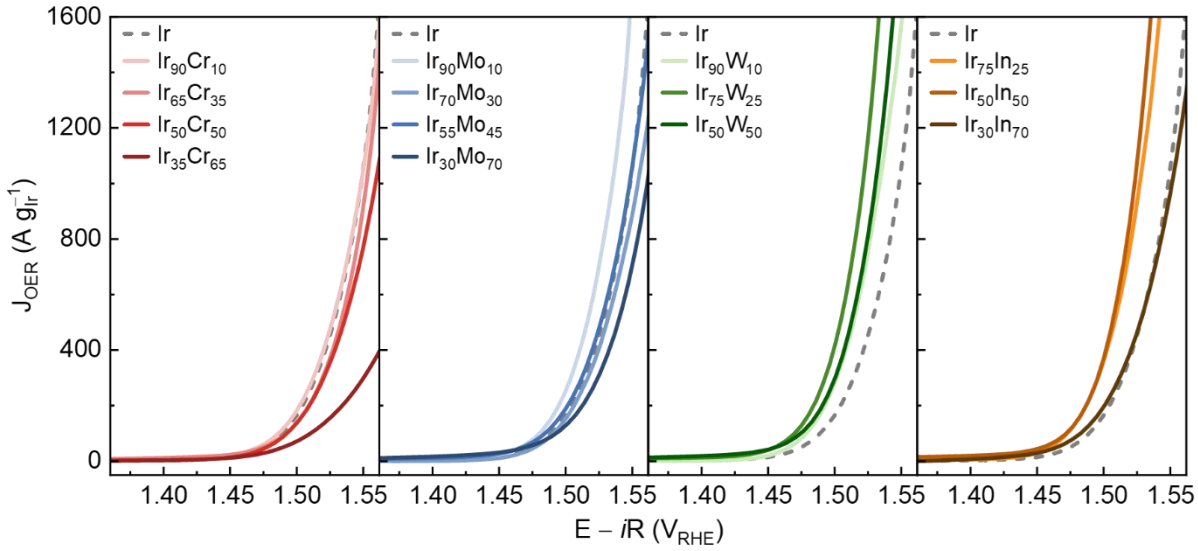

Figure S2. Ir-mass-normalized polarization curves collected for Ir and Ir-M (M = Cr, Mo, W, In) nanoparticles with various Ir/M ratios. Loading: 2 $\mu g_{catalyst}$ (catalyst : carbon black = 5 : 1 (w/w)).

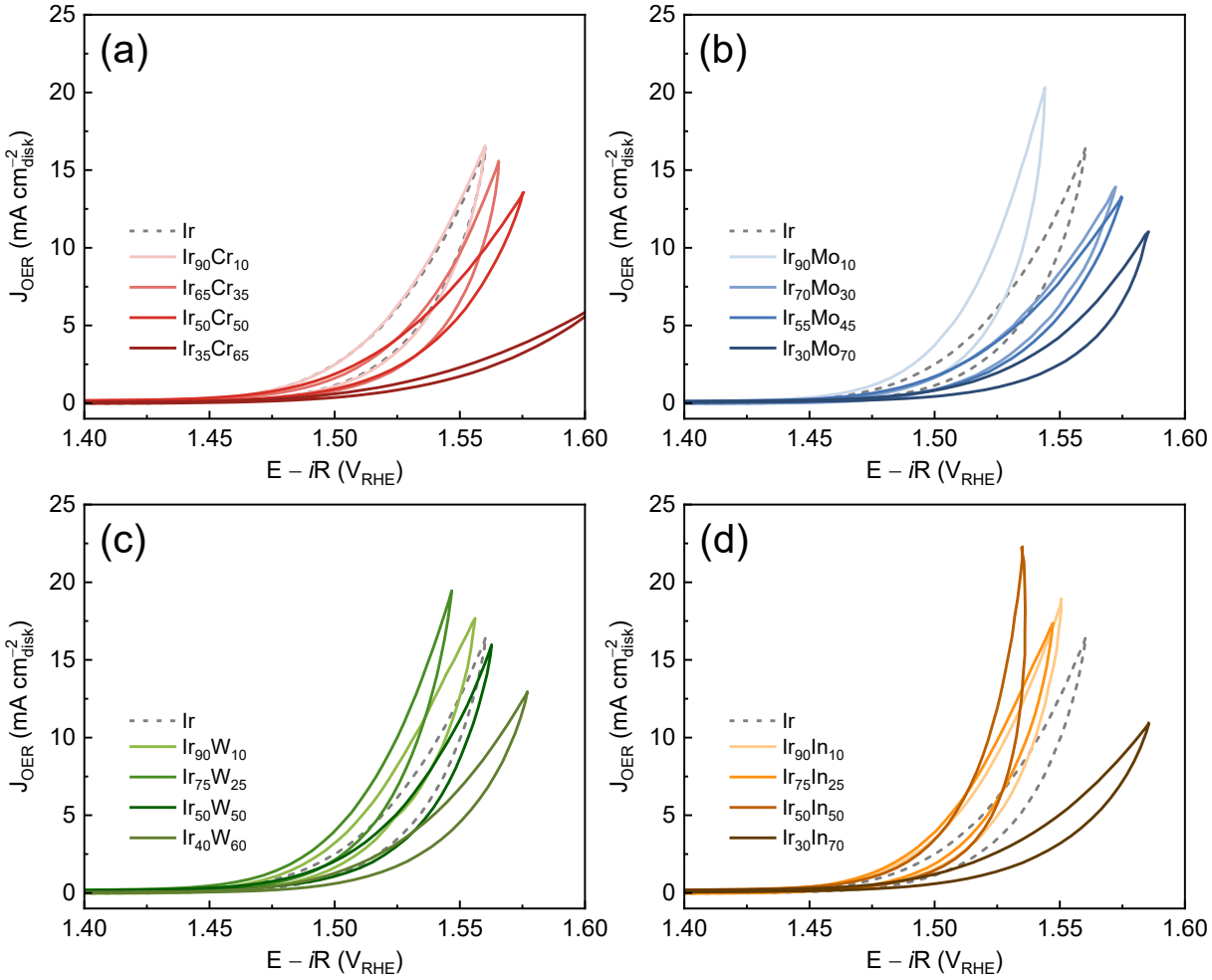

Figure S3. Cyclic voltammograms of Ir and Ir-M (M = Cr, Mo, W, In) nanoparticles with various Ir/M ratios. Loading: 2 $\mu g_{catalyst}$ (catalyst : carbon black = 5 : 1 (w/w)).

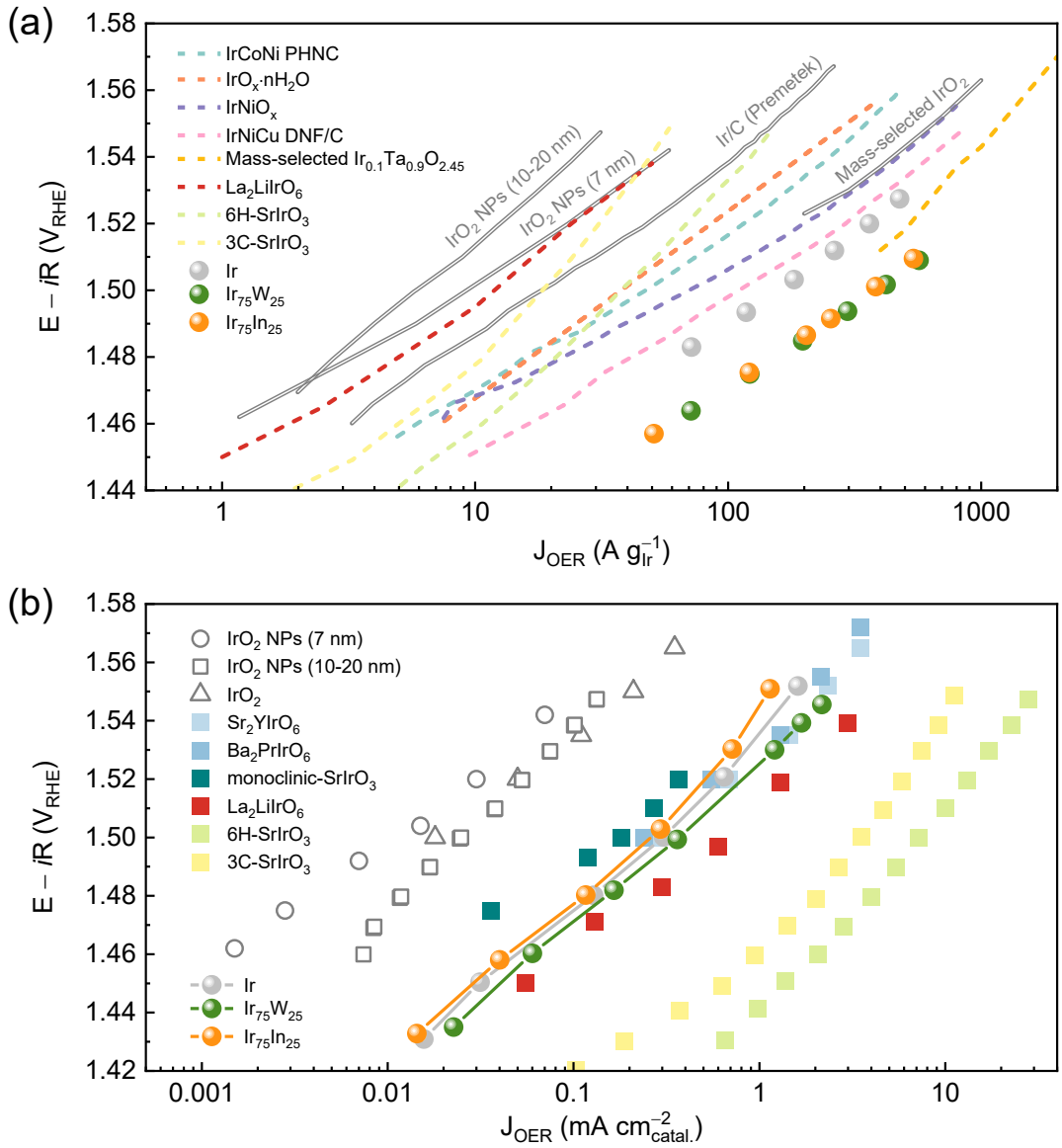

Figure S4. Comparison of acidic OER activity between Ir, $Ir_{75}W_{25}$ and $Ir_{75}In_{25}$ nanoparticles and reported Ir-based oxide catalysts based on (a) overall Ir loading and (b) geometric surface area of the catalysts. The selected references are IrO_2 nanoparticles (7 nm),[11] IrO_2 nanoparticles (10-20 nm),[12] Ir/C (Premetek),[13] IrO_2,[14] Sr_2YIrO_6 and Ba_2PrIrO_6,[14] monoclinic $SrIrO_3$,[15] 3C-$SrIrO_3$ and 6H-$SrIrO_3$,[12] La_2LiIrO_6,[16] IrCoNi PHNC,[17] $IrO_x \cdot nH_2O$,[18] $IrNiO_x$,[19] IrNiCu DNF/C,[20] and mass-selected IrO_2 and $Ir_{0.1}Ta_{0.9}O_{2.45}$.[3]

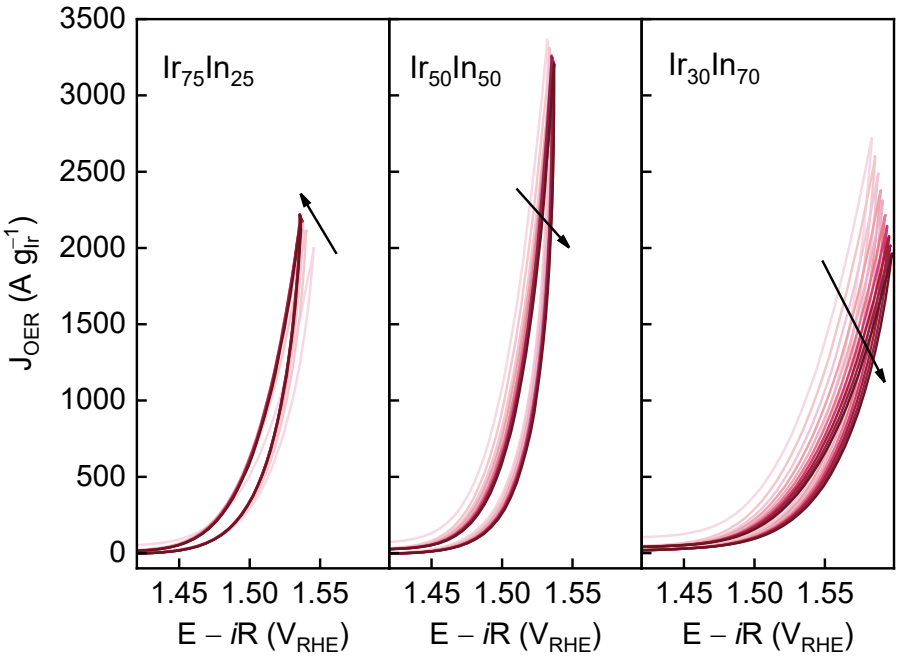

Figure S5. Cyclic voltammograms of $Ir_{75}In_{25}$, $Ir_{50}In_{50}$ and $Ir_{30}In_{70}$ nanoparticles (first 10 CV cycles are shown). Loading: 2 $\mu g_{catalyst}$ (catalyst : carbon black = 5 : 1 (w/w)). Electrolyte: 0.1 M $HClO_4$.

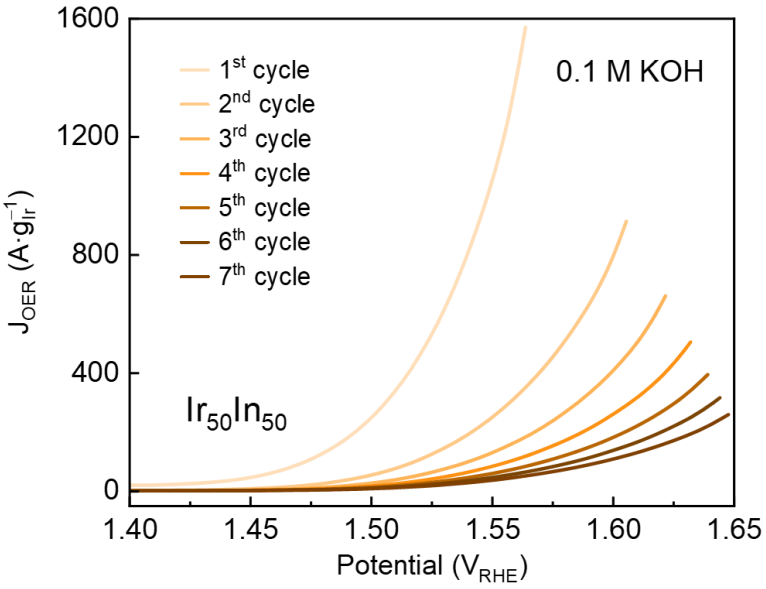

Figure S6. Cyclic voltammograms of $Ir_{50}In_{50}$ nanoparticles under alkaline OER conditions (first 7 CV cycles are shown). Loading: 2 $\mu g_{catalyst}$ (catalyst : carbon black = 5 : 1 (w/w)). Electrolyte: 0.1 M KOH (99.99%).

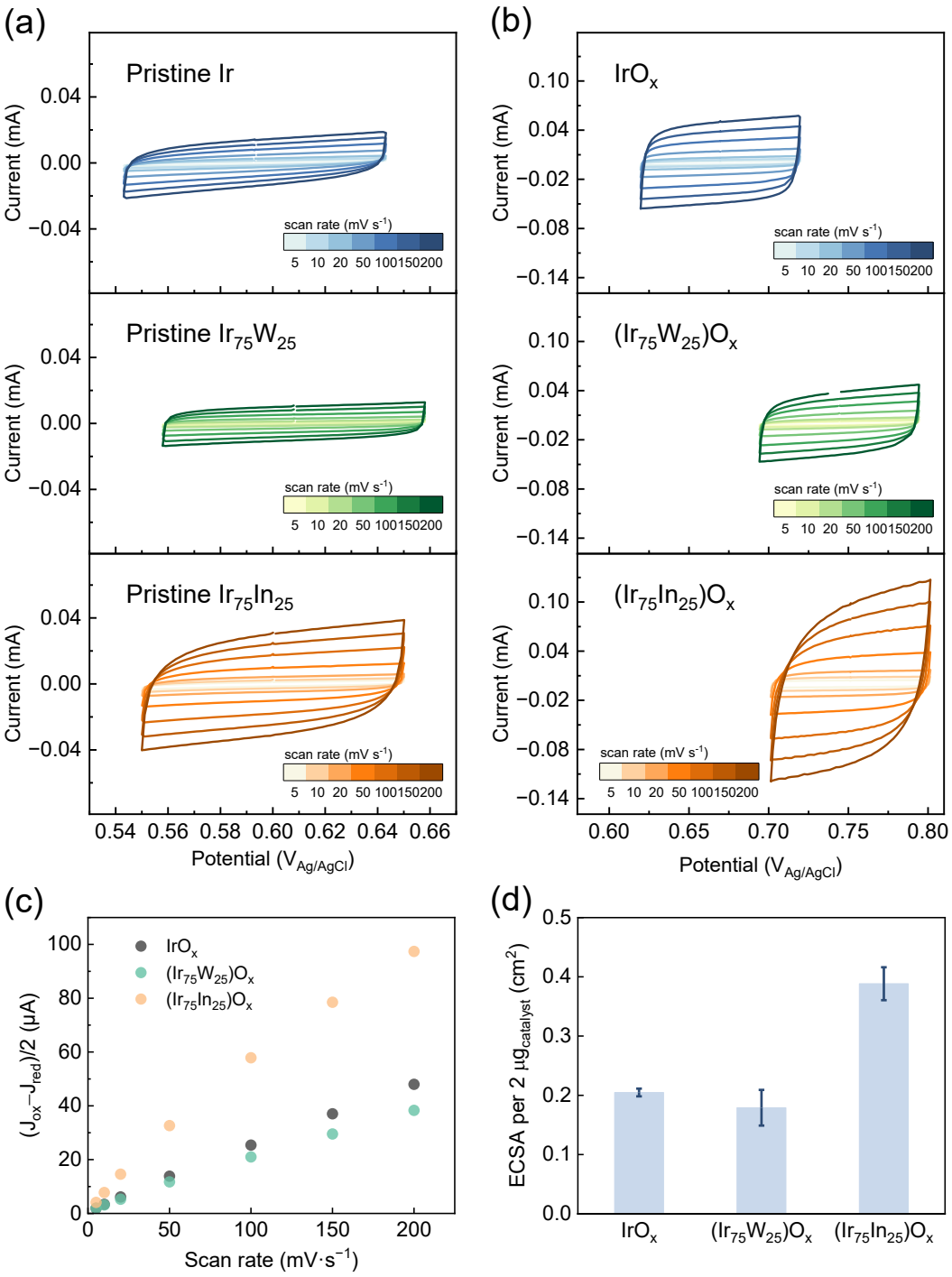

Figure S7. Electrochemical surface area (ECSA) measurements using the double layer capacitance current in O_2-saturated 0.1 M $HClO_4$. Cyclic voltammograms of (a) pristine and (b) cycled Ir, $Ir_{75}W_{25}$, and $Ir_{75}In_{25}$ nanoparticles measured in the non-Faradaic region with a scan rate ranging from 5 mV s^{-1} to 200 mV s^{-1}. (c) The averaged anodic and cathodic currents measured at an OCV at each scan rate. (d) Calculated ECSA of cycled Ir, $Ir_{75}W_{25}$, and $Ir_{75}In_{25}$ nanoparticles (mass loading: 2 $\mu g_{catalyst}$, no carbon black added).

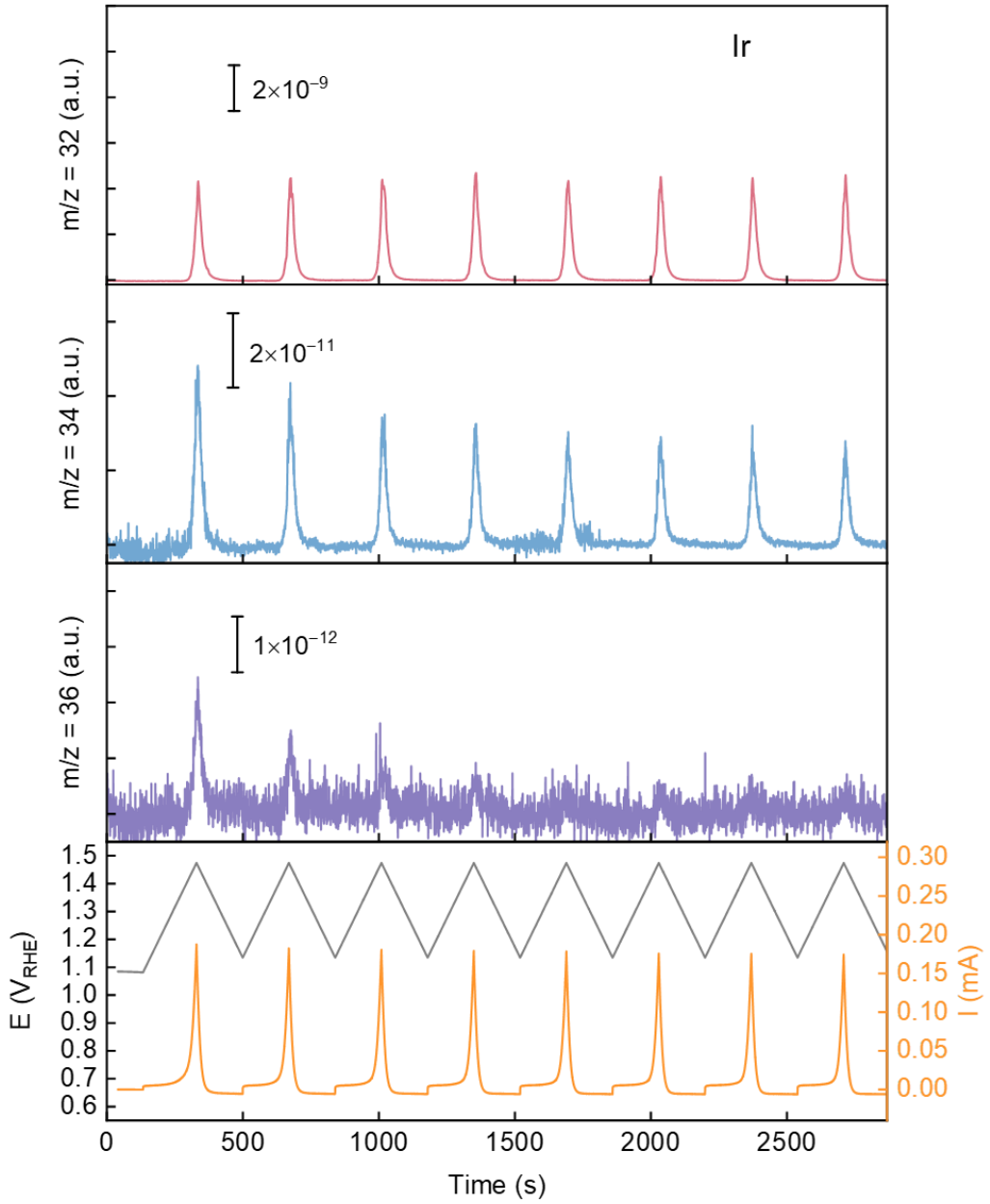

(continued)

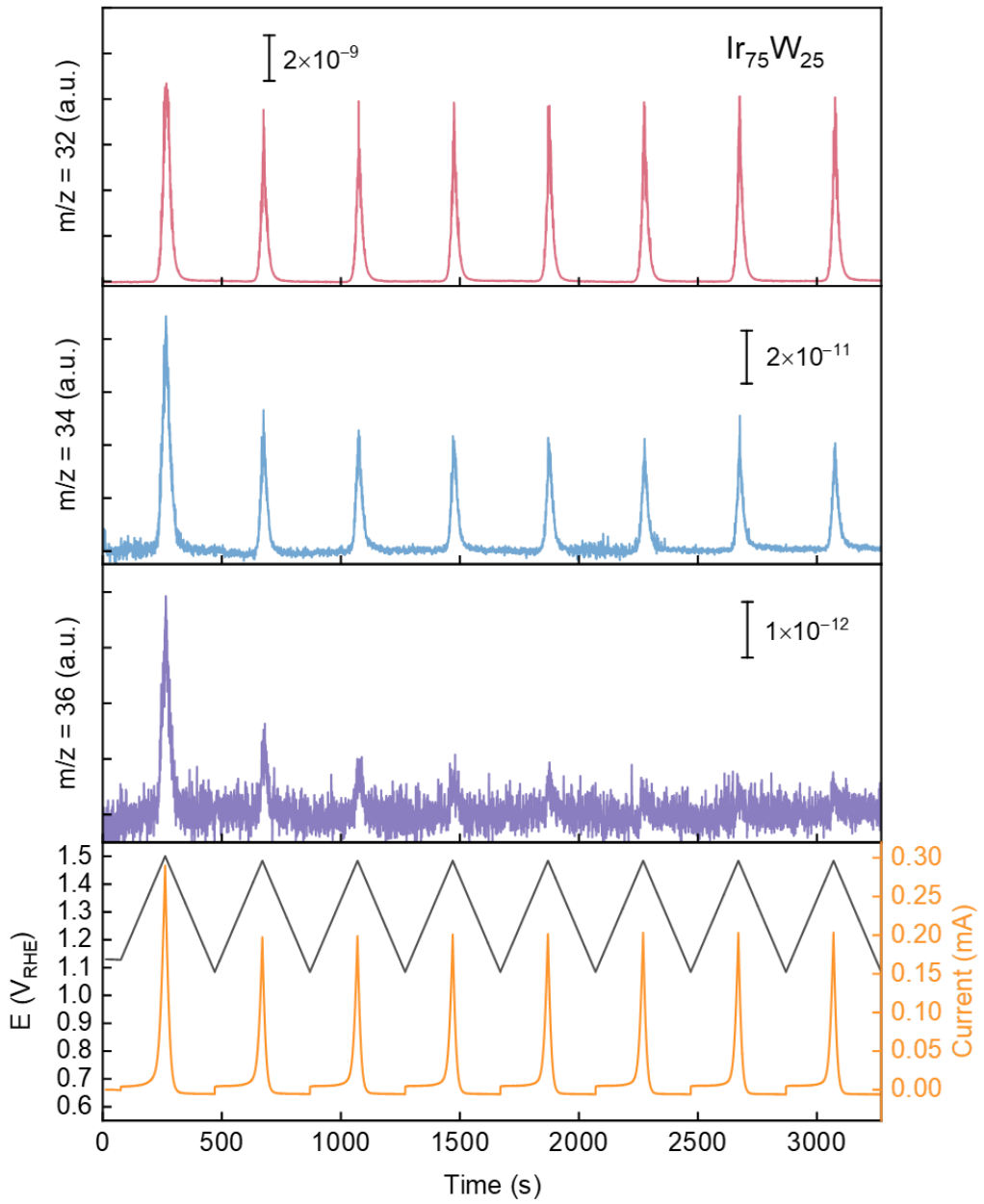
2×10⁻⁹
Ir75W25
m/z = 32 (a.u.)
2×10⁻¹¹
m/z = 34 (a.u.)
1×10⁻¹²
m/z = 36 (a.u.)
E (VRHE)
Current (mA)
Time (s)

(continued)

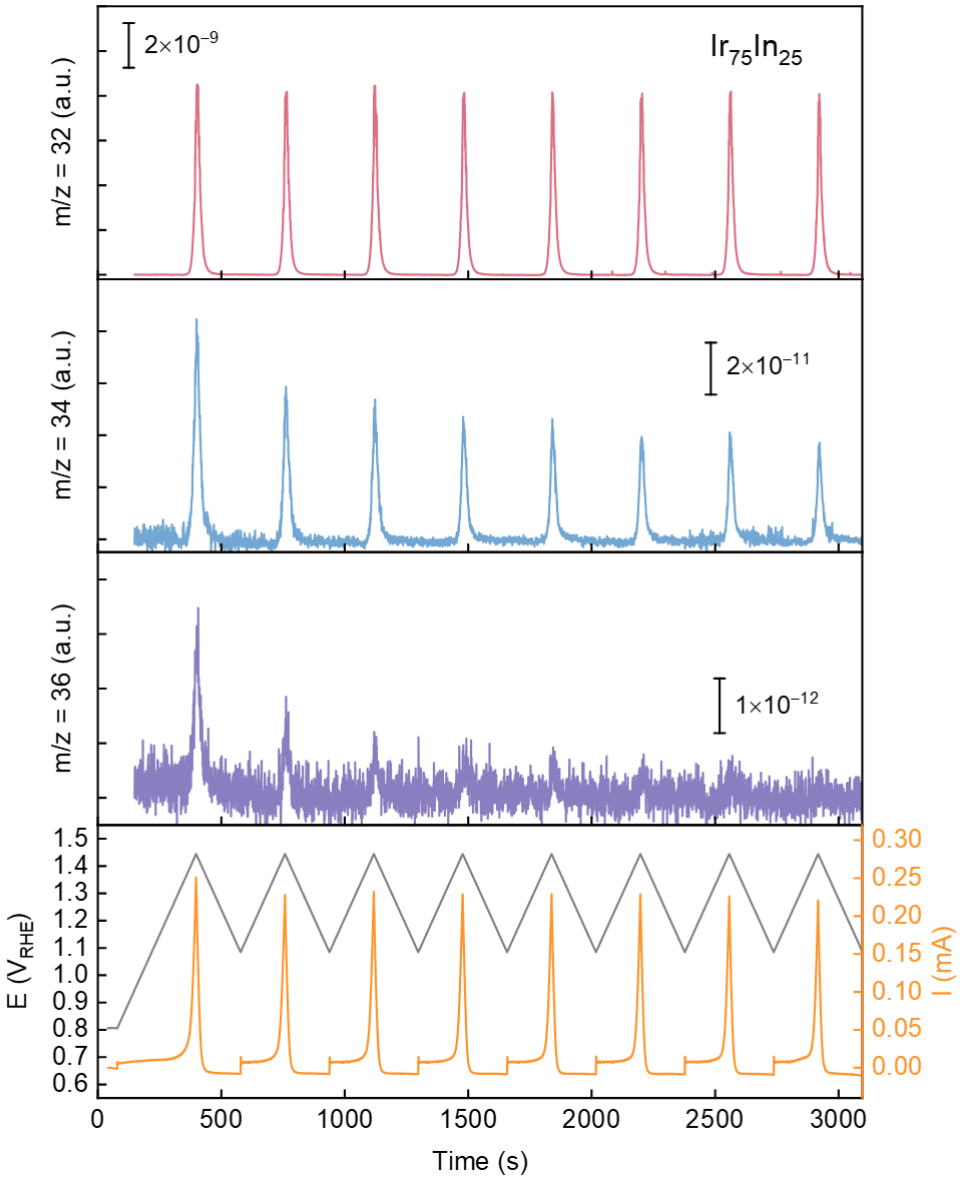

Figure S8. EC-MS profiles of current, applied potential and MS signals for m/z = 32, 34, and 36 species as a function of time during 10 CV cycles using ^{18}O-enriched Ir, $Ir_{75}W_{25}$, and $Ir_{75}In_{25}$. Electrolyte: 0.1 M $HClO_4$ in $H_2{}^{16}O$. Loading: 10 $\mu g_{catalyst}$ (on gold disk).

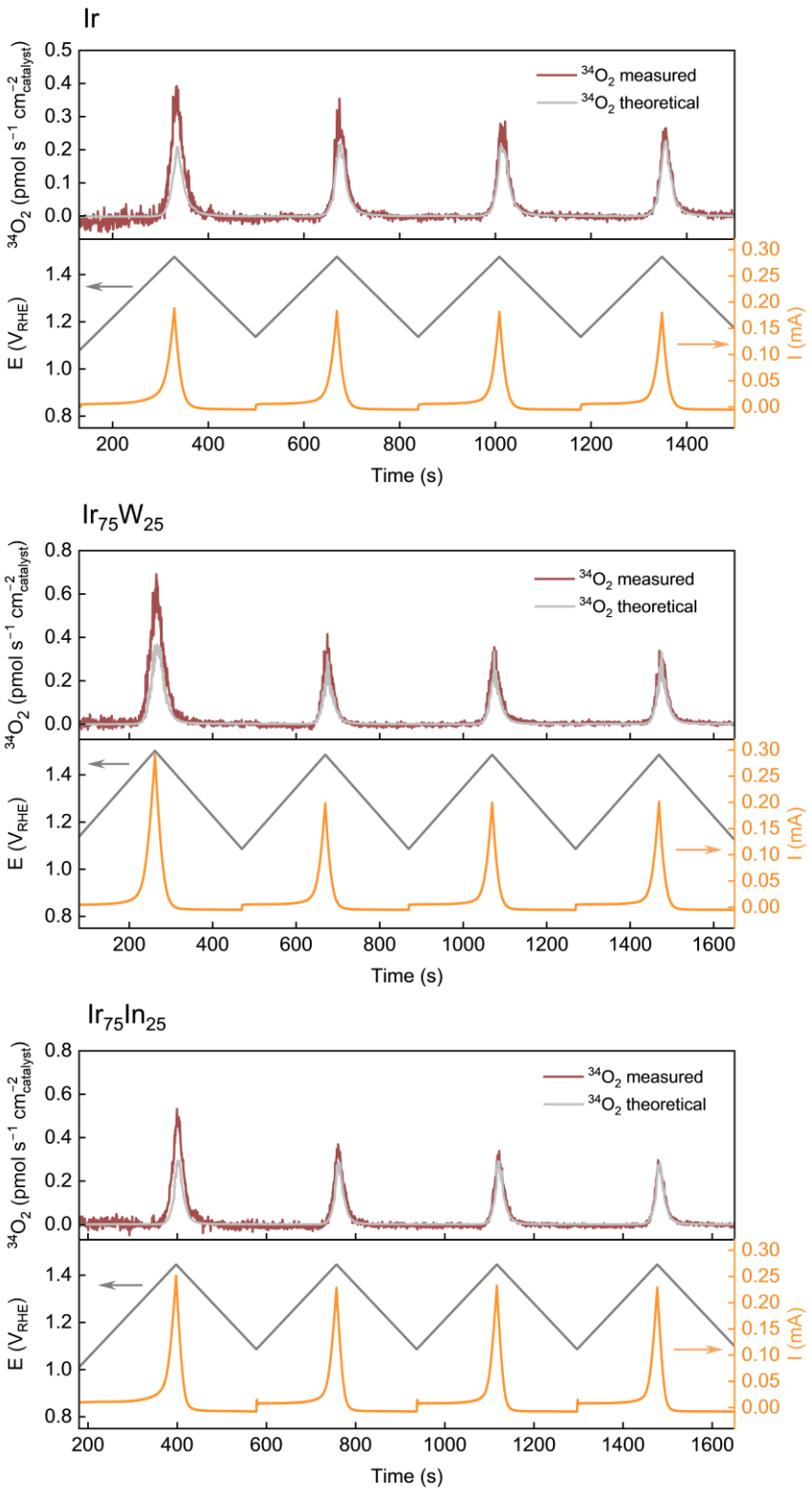

Figure S9. *Operando* EC-MS data for ^{18}O-enriched catalysts derived from metallic Ir, $Ir_{75}W_{25}$, and $Ir_{75}In_{25}$ nanoparticles, which show the comparison of the amount of $^{34}O_2$ with theoretical amount of $^{34}O_2$ calculated based on the isotopic content of ^{18}O in the electrolyte. The measurements were performed in 0.1 M $HClO_4$-^{16}O electrolyte.

From the data shown on the **Figure S9**, we calculated the excess of $^{34}O_2$ with respect to the theoretical amount based on the abundance of the isotope ^{18}O in the electrolyte. It should be noted that the data for $^{34}O_2$ were scaled using the experimentally observed steady-state $^{32}O_2/^{34}O_2$ ratio (168–184 for Ir, IrW and IrIn) obtained during the galvanostatic experiments at a high current density (0.5 mA cm^{-2}) (to ensure depletion of the ^{18}O label on the catalyst surface), instead of using the theoretical value of $^{32}O_2/^{34}O_2 = 250$ [ref.[21]], to account for any possible contamination of the electrolyte with the ^{18}O label above the natural abundance level and hence to avoid an overestimation of the lattice oxygen evolution. It was found that the excess of ^{18}O evolved from the lattice in form of $^{34}O_2$ during the first CV cycle (1.2 V_{RHE} – 1.47 V_{RHE}, 2 mV s^{-1}) on Ir, IrW and IrIn corresponds to ~ 0.04 – 0.3 % of the total oxygen atoms in the catalyst lattice and 0.2 – 0.6 % of the oxygen atoms on the catalyst's surface monolayer (calculated (1) based on the known mean particle diameters, assuming a spherical shape; (2) using the crystallographic parameters of the (010) plane of rutile IrO_2; (3) assuming that all oxygen in the catalyst is present as ^{18}O after labelling). These data indicate that the lattice oxygen evolution is a rather minor reaction pathway; this conclusion is consistent with previous studies on sputtered IrO_x films which also demonstrate a negligible role of the pathways involving lattice oxygen in the overall OER activity.[22]

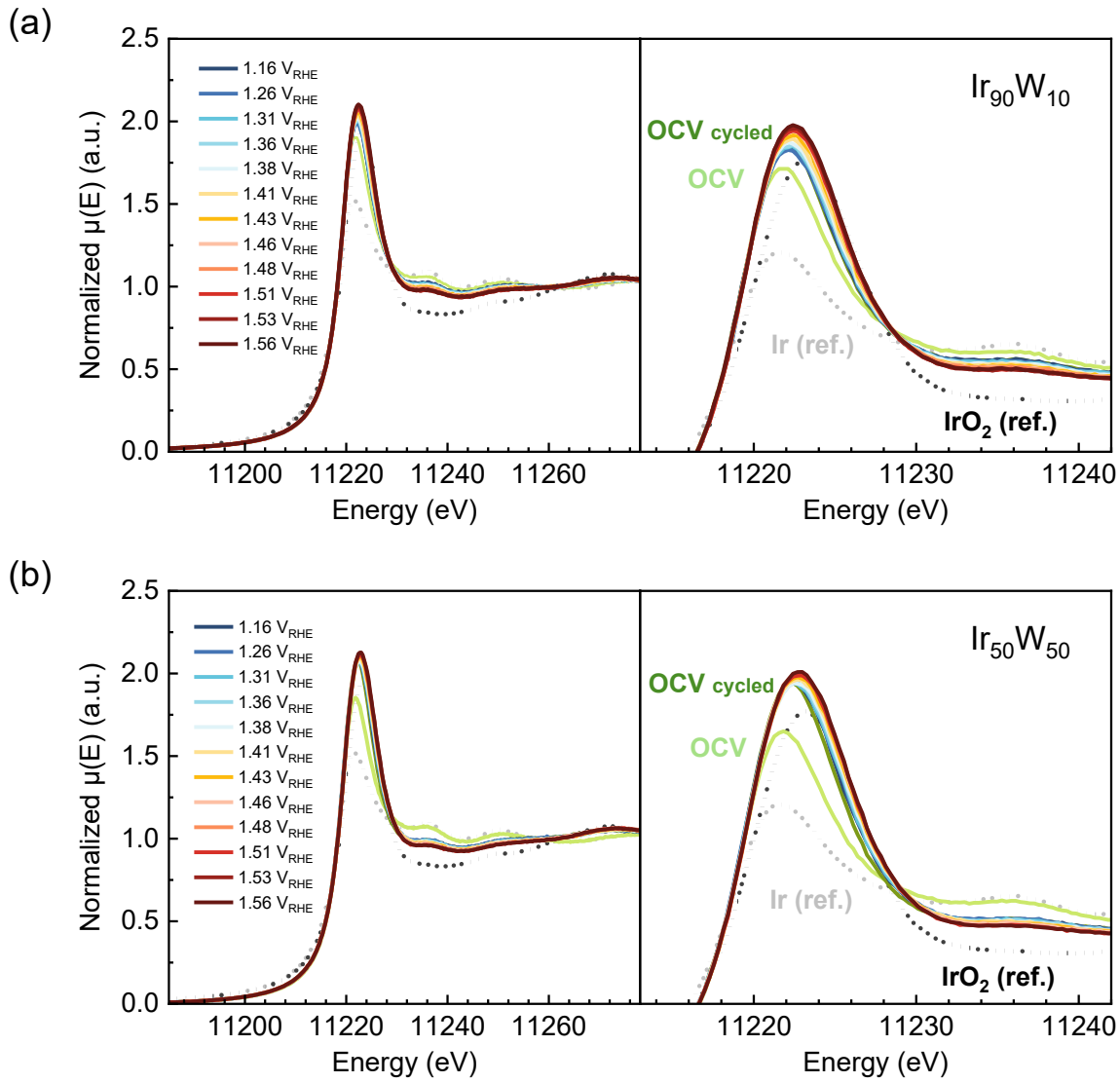

Figure S10. *In situ* Ir L_3-edge XANES spectra of (a) $Ir_{90}W_{10}$ and (b) $Ir_{50}W_{50}$ and the reference materials.

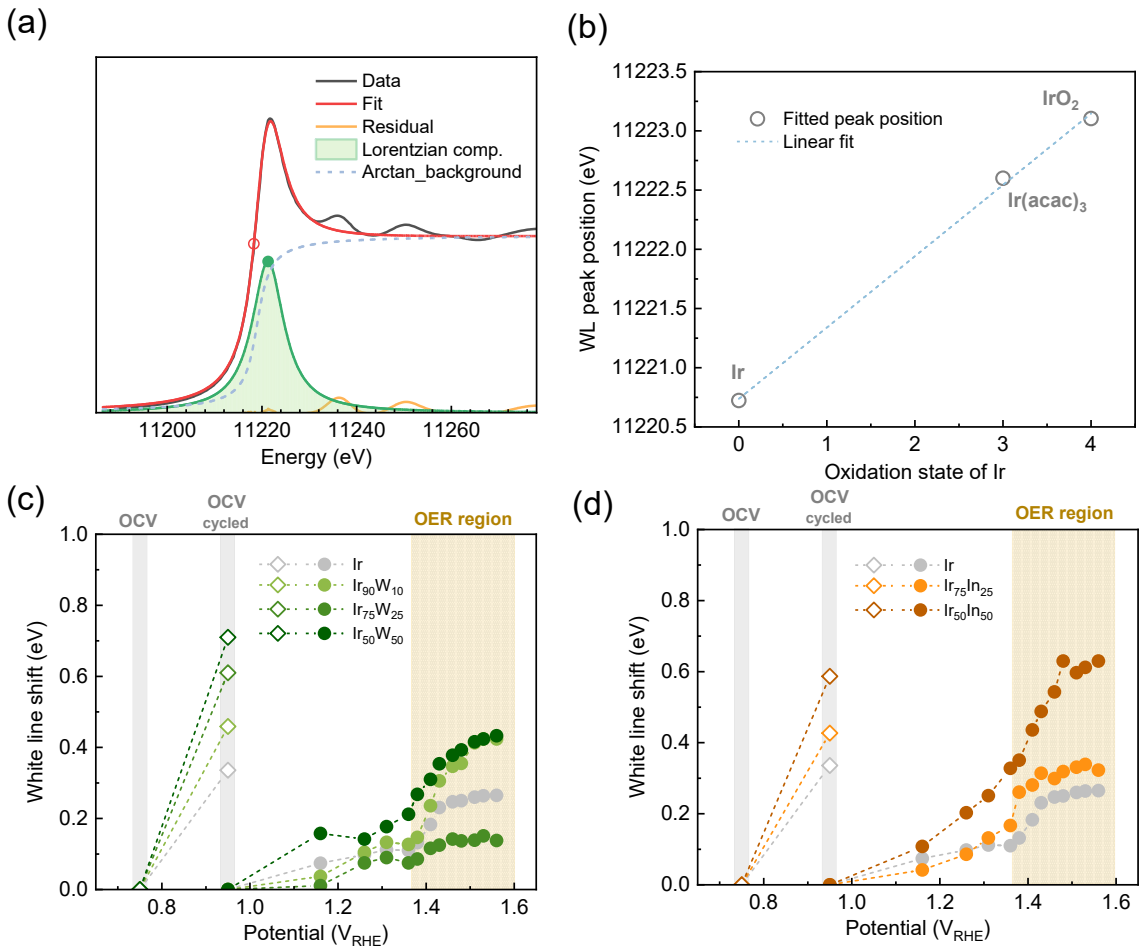

Figure S11. (a) Schematic of the Ir L_3-edge white-line peak fitting approach. (b) White line position of the Ir references as a function of the formal oxidation state of Ir. Fitted white line peak shift of (c) Ir-W and (d) Ir-In nanoparticles during the *in situ* experiments. The hollow rhombus symbols represent the white line peak shift before and after cycling; the solid circle symbols represent the white line peak shift during potentiostatic steps.

The red circle in **Figure S11a** indicates the inflection point of the first-derivative of the raw spectrum, which is the center of the arctangent background. The maximum of a single Lorentzian-shaped component is given as the solid green circle. Note that the oxidation state deduced from the fitting of the white line peak position represents the average oxidation state of Ir in the catalyst, *i.e.*, includes metallic Ir and IrO_x.

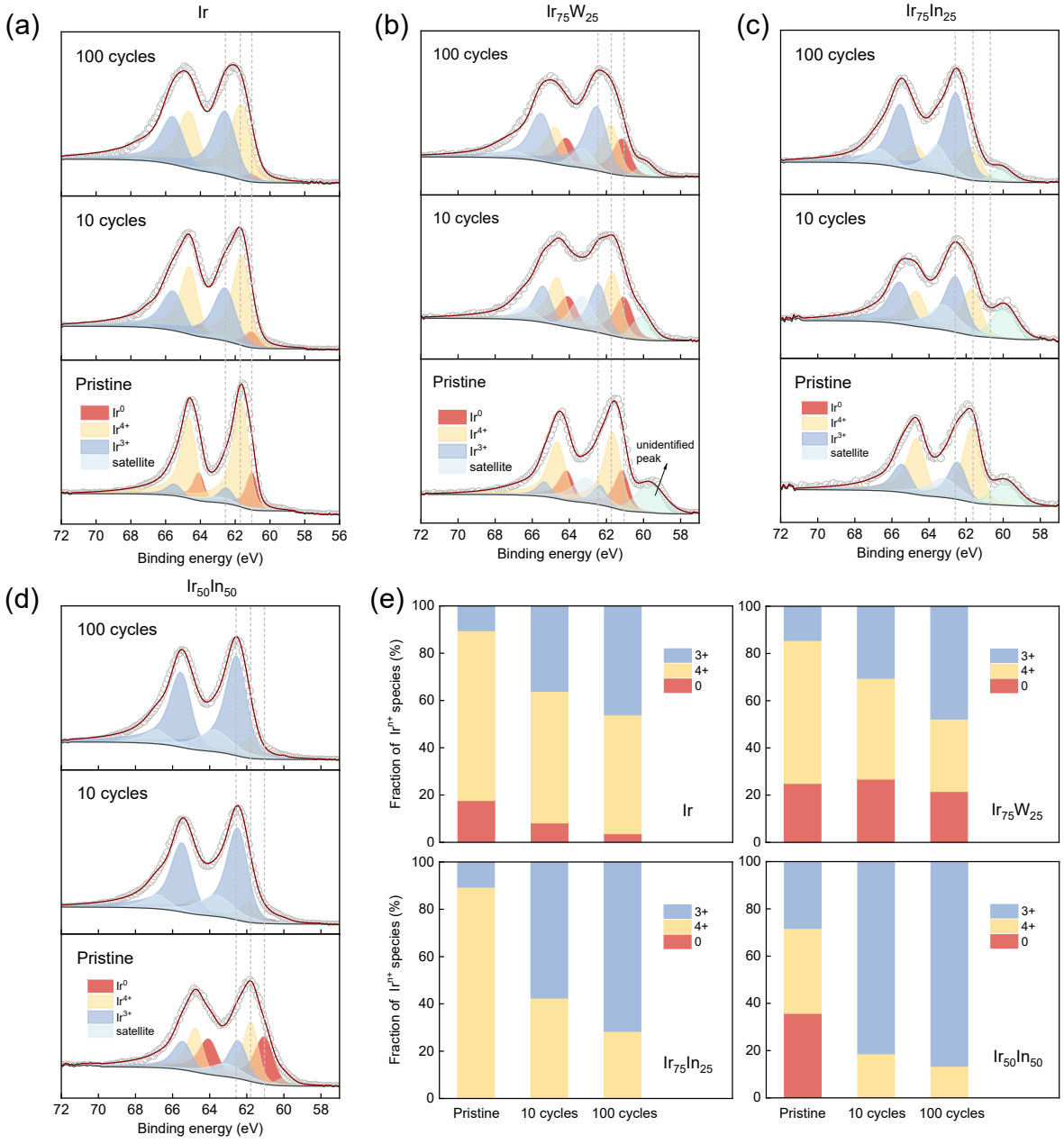

Figure S12. *Ex situ* X-ray photoelectron Ir *4f* core spectra of pristine and cycled (a) monometallic Ir, (b) $Ir_{75}W_{25}$, (c) $Ir_{75}In_{25}$, and (d) $Ir_{50}In_{50}$ nanoparticles. (e) The determined surface composition of Ir^0, Ir^{3+} and Ir^{4+} species in the nanoparticles at different reaction stages.

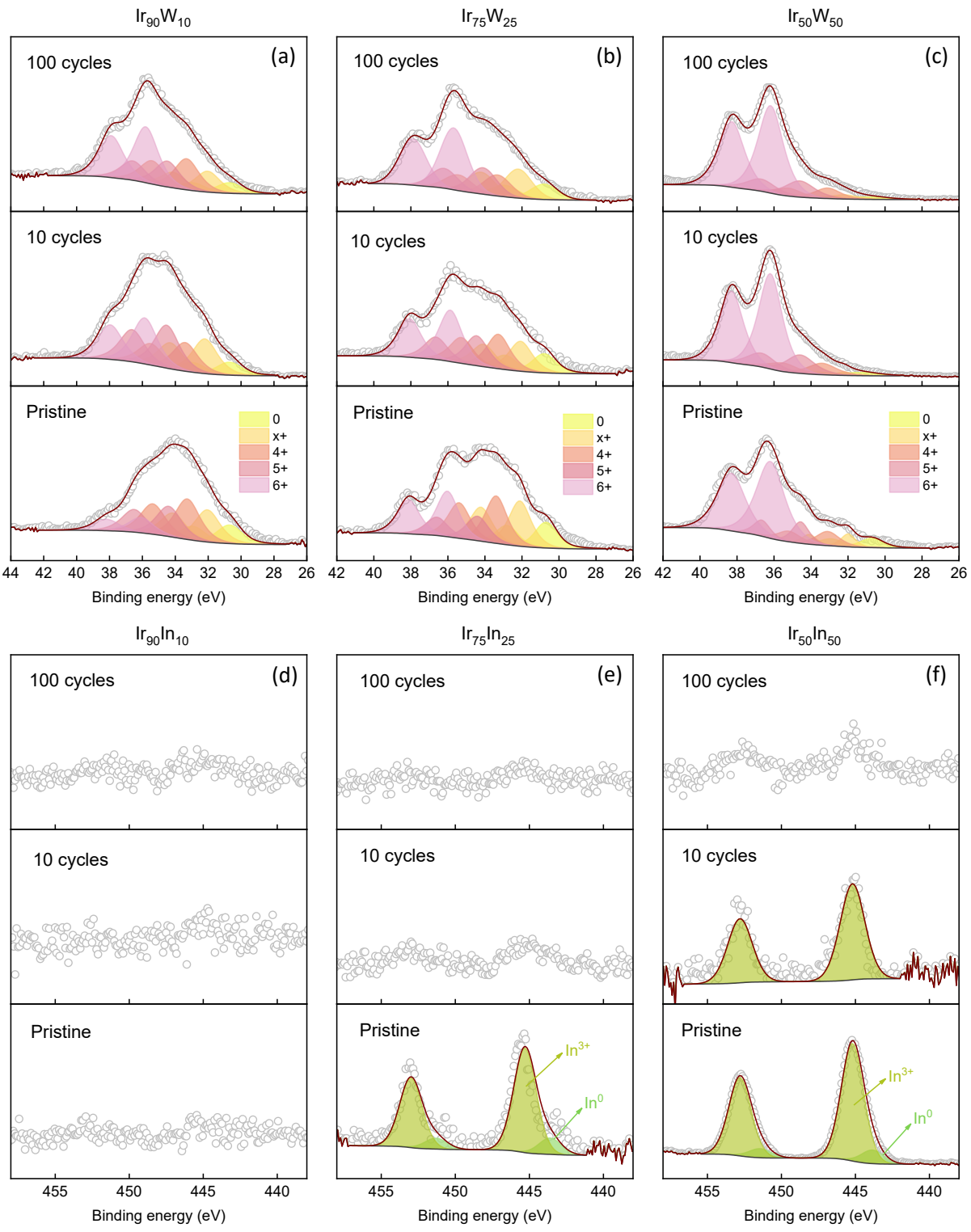

Figure S13. *Ex situ* X-ray photoelectron W *4f* core spectra of (a) $Ir_{90}W_{10}$, (b) $Ir_{75}W_{25}$, and (c) $Ir_{50}W_{50}$ and In *3d* core spectra of (d) $Ir_{90}In_{10}$, (e) $Ir_{75}In_{25}$, and (f) $Ir_{50}In_{50}$ at different reaction stages. The W^{x+} component in the W 4*f* core region represents W species with oxidation states below 4+.[23]

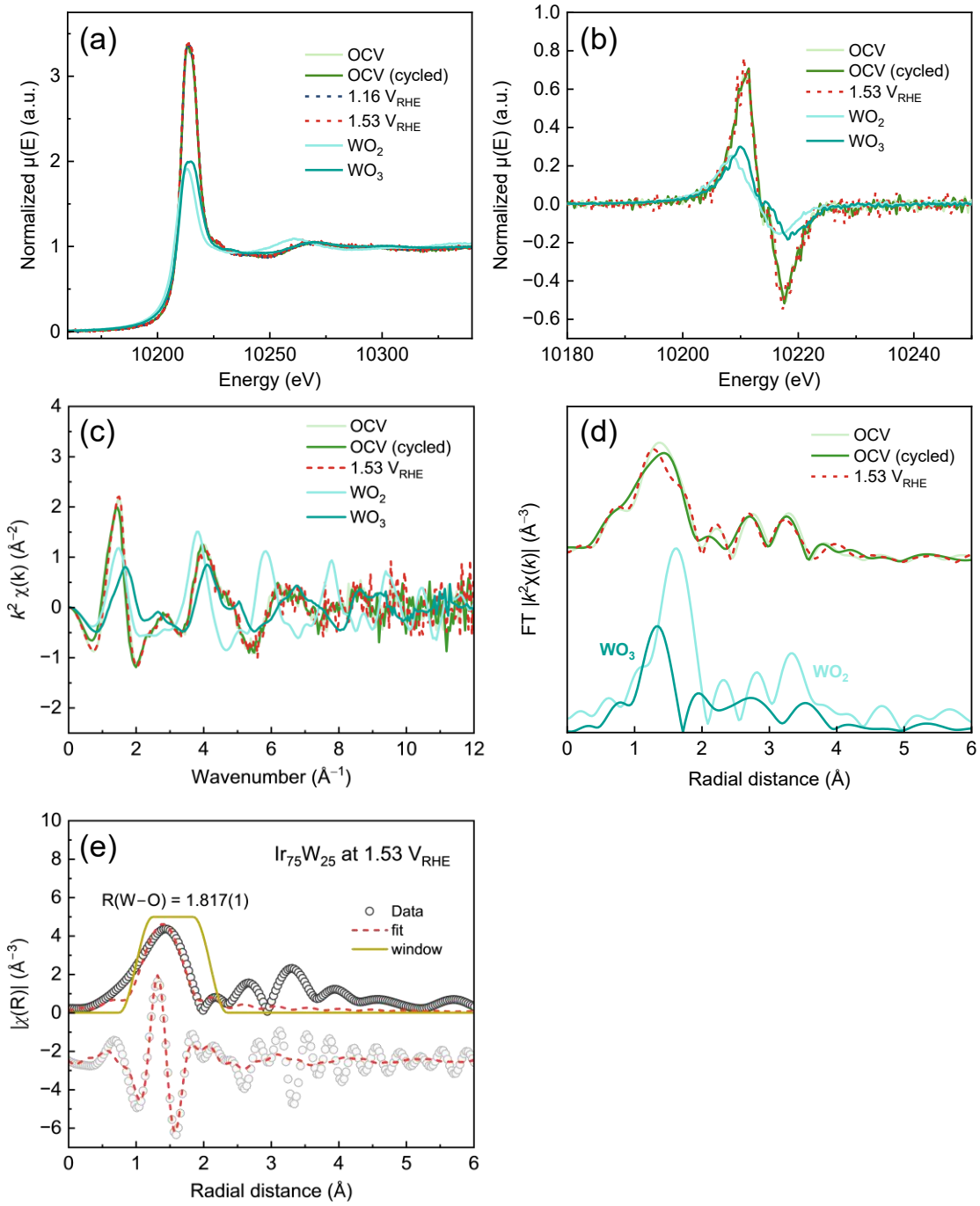

Figure S14. *In situ* W L_3-edge (a) XANES spectra, (b) first derivative of the XANES region, (c) EXAFS k^2 χ(k) spectra and (d) the Fourier-transform of k^2 χ(k) spectra of $Ir_{75}W_{25}$. (e) The experimental and fitted Fourier transform of the EXAFS data of $Ir_{75}W_{25}$ at 1.53 V_{RHE} for an R-space of 1.0 – 2.0 Å and k-space range of 3.0 – 9.0 Å^{-1} (using Hanning window, dk=0.5 Å^{-1}, dR=0.5 Å, S_0=0.7, σ^2 = 0.005) with the single scattering path of O6.1 in WO_3 (CIF 84140).

The fitted R(W−O) = 1.817(1) Å (of W-species in $Ir_{75}W_{25}$) is between that of $W^{4+}O_2$ (R(W−O) = 1.927 Å) and $W^{6+}O_3$ (R(W−O) = 1.744 Å), implying the mean oxidation state of W is between +4 and +6 (in good agreement with *ex situ* XPS data, **Figure S13**) .

The peak at *ca.* 2.7 Å (without phase correction) originated from multiple scattering processes within the first shell of the W-O octahedra.[24] The W−W shell at *ca.* 3.3 Å (without phase correction) is assigned to edge-shared W-O octahedra, whereas the absence of W neighbours at 3.7 Å (without phase correction, corner-shared octahedra) supports the fact that no crystalline WO_x phases are formed.[25, 26] These features indicate that the local environment of W in IrO_x:W is different from that of WO_2 and WO_3.

Table S2. *In situ* Ir L_3-edge EXAFS best-fit parameters for the Ir, Ir-W and Ir-In catalysts for an R-space of 1.1–3.0 Å and k-space range of 3.0–12.5 $Å^{-1}$ (using Hanning window, dk=0.5 $Å^{-1}$, dR=0.5 Å and S_0=0.67). The Debye–Waller factors (σ^2) of the Ir–O and Ir–M shells were fixed to 0.005 and 0.004, respectively (except for $Ir_{50}W_{50}$ and $Ir_{50}In_{50}$). ΔE(Ir–M) was defined as ΔE(Ir–O).

Material	Scattering path	Reaction stage	CN	σ^2 ($Å^2$)	ΔE (eV)	R (Å)	R factor
Ir	Ir–O	OCV	1.1(1)	0.005	8.1(6)	1.95(1)	0.003
		OCV (cycled)	2.0(1)		7.4(6)	1.958(8)	0.003
		1.16 V_{RHE}	2.1(2)		6(1)	1.95(1)	0.008
		1.26 V_{RHE}	2.2(2)		7(1)	1.95(1)	0.007
		1.31 V_{RHE}	2.2(1)		7.2(7)	1.944(8)	0.004
		1.36 V_{RHE}	2.2(2)		7(1)	1.94(1)	0.011
		1.38 V_{RHE}	2.2(2)		7(1)_	1.95(1)	0.011
		1.41 V_{RHE}	2.3(2)		7(1)	1.95(1)	0.008
		1.43 V_{RHE}	2.4(2)		7.0(9)	1.943(9)	0.007
		1.46 V_{RHE}	2.4(2)		7(1)	1.94(1)	0.010
		1.48 V_{RHE}	2.6(2)		7.6(1)	1.953(9)	0.007
		1.51 V_{RHE}	2.4(2)		7(1)	1.94(1)	0.009
		1.56 V_{RHE}	2.5(3)		6(1)	1.94(1)	0.003
	Ir–M	OCV	10.4(2)	0.004	8.1(6)	2.700(2)	0.003
		OCV (cycled)	8.6(2)		7.4(6)	2.698(3)	0.003
		1.16 V_{RHE}	8.2(3)		6(1)	2.694(4)	0.008
		1.26 V_{RHE}	8.1(3)		7(1)	2.699(4)	0.007
		1.31 V_{RHE}	8.5(2)		7.2(7)	2.698(3)	0.004
		1.36 V_{RHE}	7.9(3)		7(1)	2.696(5)	0.011
		1.38 V_{RHE}	7.8(3)		7(1)	2.700(5)	0.011
		1.41 V_{RHE}	7.9(3)		7(1)	2.700(4)	0.008
		1.43 V_{RHE}	7.9(3)		7.0(9)	2.699(4)	0.007
		1.46 V_{RHE}	7.5(3)		7(1)	2.699(5)	0.010
		1.48 V_{RHE}	7.6(3)		7.6(1)	2.700(4)	0.007
		1.51 V_{RHE}	7.5(3)		7(1)	2.698(5)	0.009
		1.56 V_{RHE}	7.5(4)		6(1)	2.689(6)	0.003
$Ir_{90}W_{10}$	Ir–O	OCV	1.4(7)	0.008	7(1)	1.96(2)	0.006
		OCV (cycled)	2.2(3)	0.005	7(1)	1.96(1)	0.021
		1.16 V_{RHE}	2.2(3)		7(1)	1.96(1)	0.025
		1.26 V_{RHE}	2.3(3)		8(1)	1.96(1)	0.022
		1.31 V_{RHE}	2.2(3)		6(1)	1.95(1)	0.024

		1.36 V_{RHE}	2.5(3)		7(2)	1.96(1)	0.035
		1.38 V_{RHE}	2.7(3)		8(1)	1.97(1)	0.027
		1.41 V_{RHE}	2.7(3)		8(2)	1.96(1)	0.036
		1.43 V_{RHE}	2.9(3)		7(2)	1.96(1)	0.036
		1.46 V_{RHE}	3.0(3)		7(2)	1.95(1)	0.039
		1.48 V_{RHE}	3.1(3)		8(1)	1.96(1)	0.033
		1.51 V_{RHE}	3.2(3)		8(2)	1.96(1)	0.042
		1.53 V_{RHE}	3.3(3)		8(1)	1.96(1)	0.032
		1.56 V_{RHE}	3.2(3)		7(1)	1.95(1)	0.034
	Ir–M	OCV	10.0(8)	0.005	7(1)	2.697(4)	0.006
		OCV (cycled)	6.6(4)	0.004	7(1)	2.695(6)	0.021
		1.16 V_{RHE}	6.3(4)		7(1)	2.691(7)	0.025
		1.26 V_{RHE}	6.3(4)		8(1)	2.695(6)	0.022
		1.31 V_{RHE}	6.4(4)		6(1)	2.692(7)	0.024
		1.36 V_{RHE}	5.9(5)		7(2)	2.696(8)	0.035
		1.38 V_{RHE}	6.0(4)		8(1)	2.699(7)	0.027
		1.41 V_{RHE}	5.3(5)		8(2)	2.697(9)	0.036
		1.43 V_{RHE}	5.4(5)		7(2)	2.691(9)	0.036
		1.46 V_{RHE}	5.2(5)		7(2)	2.692(9)	0.039
		1.48 V_{RHE}	5.0(4)		8(1)	2.699(8)	0.033
		1.51 V_{RHE}	4.9(5)		8(2)	2.69(1)	0.042
		1.53 V_{RHE}	4.8(4)		8(1)	2.698(8)	0.032
		1.56 V_{RHE}	5.0(5)		7(1)	2.693(8)	0.034
$Ir_{75}W_{25}$	Ir–O	OCV	1.2(5)	0.005	7(1)	1.97(3)	0.0032
		OCV (cycled)	2.7(4)		8(2)	1.97(2)	0.0041
		1.16 V_{RHE}	2.9(4)		8(2)	1.97(2)	0.040
		1.26 V_{RHE}	3.0(5)		8(2)	1.97(2)	0.048
		1.31 V_{RHE}	2.8(4)		8(2)	1.96(2)	0.040
		1.36 V_{RHE}	2.9(4)		8(2)	1.96(2)	0.043
		1.38 V_{RHE}	2.8(4)		7(2)	1.95(1)	0.040
		1.41 V_{RHE}	2.9(4)		9(2)	1.97(2)	0.047
		1.43 V_{RHE}	2.9(4)		8(2)	1.96(1)	0.039
		1.46 V_{RHE}	3.1(4)		8(2)	1.96(1)	0.038
		1.48 V_{RHE}	3.0(3)		9(2)	1.97(1)	0.033
		1.51 V_{RHE}	3.2(4)		9(2)	1.97(1)	0.042
		1.53 V_{RHE}	3.2(4)		11(2)	1.99(1)	0.039
		1.56 V_{RHE}	3.0(4)		9(2)	1.96(1)	0.037
	Ir–M	OCV	9.7(7)	0.004	7(1)	2.698(8)	0.0032
		OCV (cycled)	6.5(6)		8(2)	2.70(1)	0.0041

		1.16 V_{RHE}	6.8(6)		8(2)	2.705(9)	0.040
		1.26 V_{RHE}	7.0(7)		8(2)	2.70(1)	0.048
		1.31 V_{RHE}	6.6(6)		8(2)	2.704(9)	0.040
		1.36 V_{RHE}	6.4(6)		8(2)	2.70(1)	0.043
		1.38 V_{RHE}	6.3(6)		7(2)	2.699(9)	0.040
		1.41 V_{RHE}	6.2(6)		9(2)	2.70(1)	0.047
		1.43 V_{RHE}	6.2(6)		8(2)	2.701(9)	0.039
		1.46 V_{RHE}	5.9(6)		8(2)	2.702(9)	0.038
		1.48 V_{RHE}	6.1(5)		9(2)	2.705(9)	0.033
		1.51 V_{RHE}	5.8(6)		9(2)	2.70(1)	0.042
		1.53 V_{RHE}	5.7(6)		11(2)	2.71(1)	0.039
		1.56 V_{RHE}	6.0(5)		9(2)	2.703(9)	0.037
$Ir_{50}W_{50}$	Ir–O	OCV	2.7(7)	0.005	7.3(7)	2.67(2)	0.035
		OCV (cycled)	3.3(3)		12(2)	2.01(1)	0.033
		1.16 V_{RHE}	3.2(3)		11(2)	1.99(1)	0.036
		1.26 V_{RHE}	3.0(3)		8(2)	1.97(1)	0.041
		1.31 V_{RHE}	3.1(3)		8(2)	1.96(1)	0.035
		1.36 V_{RHE}	3.2(3)		9(1)	1.96(1)	0.031
		1.38 V_{RHE}	3.2(4)		8(2)	1.96(1)	0.050
		1.41 V_{RHE}	3.3(3)		10(2)	1.98(1)	0.040
		1.43 V_{RHE}	3.5(3)		11(2)	1.98(1)	0.037
		1.46 V_{RHE}	3.6(4)		10(2)	1.97(1)	0.055
		1.51 V_{RHE}	3.7(3)		8(2)	1.95(1)	0.044
		1.56 V_{RHE}	3.6(3)		7(2)	1.95(1)	0.041
	Ir–M	OCV	8.4(6)	0.004	7.3(7)	2.553(9)	0.035
		OCV (cycled)	4.8(4)		12(2)	2.716(9)	0.033
		1.16 V_{RHE}	5.0(5)		11(2)	2.712(9)	0.036
		1.26 V_{RHE}	5.0(5)		8(2)	2.703(9)	0.041
		1.31 V_{RHE}	5.1(5)		8(2)	2.702(9)	0.035
		1.36 V_{RHE}	4.8(4)		9(1)	2.703(8)	0.031
		1.38 V_{RHE}	4.7(5)		8(2)	2.69(1)	0.050
		1.41 V_{RHE}	4.6(5)		10(2)	2.71(1)	0.040
		1.43 V_{RHE}	4.5(5)		11(2)	2.714(9)	0.037
		1.46 V_{RHE}	3.9(6)		10(2)	2.70(1)	0.055
		1.51 V_{RHE}	4.1(5)		8(2)	2.69(1)	0.044
		1.56 V_{RHE}	4.1(5)		7(2)	2.69(1)	0.041
$Ir_{75}In_{25}$	Ir–O	OCV	3.7(2)	0.005	12(1)	2.02(1)	0.022
		OCV (cycled)	4.8(3)		10(1)	2.00(1)	0.024
		1.16 V_{RHE}	4.9(3)		11(1)	2.01(1)	0.026

		1.26 V_{RHE}	4.8(3)		10(2)	2.00(1)	0.032
		1.31 V_{RHE}	4.9(3)		9(1)	1.99(1)	0.027
		1.36 V_{RHE}	4.9(3)		10(1)	1.99(1)	0.030
		1.38 V_{RHE}	4.9(4)		11(2)	2.00(1)	0.038
		1.41 V_{RHE}	5.0(3)		10(1)	1.99(1)	0.030
		1.43 V_{RHE}	5.1(3)		10(1)	1.99(1)	0.031
		1.46 V_{RHE}	5.3(3)		9(1)	1.98(1)	0.023
		1.48 V_{RHE}	5.2(4)		10(1)	1.99(1)	0.035
		1.51 V_{RHE}	5.2(3)		10(1)	1.99(1)	0.031
		1.53 V_{RHE}	5.3(3)		10(1)	1.99(1)	0.027
		1.56 V_{RHE}	5.4(3)		10(1)	1.99(1)	0.029
	Ir–M	OCV	3.4(4)	0.004	12(1)	2.69(1)	0.022
		OCV (cycled)	1.9(5)		10(1)	2.69(1)	0.024
		1.16 V_{RHE}	2.0(4)		11(1)	2.69(1)	0.026
		1.26 V_{RHE}	1.9(5)		10(2)	2.68(1)	0.032
		1.31 V_{RHE}	1.8(5)		9(1)	2.68(1)	0.027
		1.36 V_{RHE}	1.7(5)		10(1)	2.69(1)	0.030
		1.38 V_{RHE}	1.4(5)		11(2)	2.68(2)	0.038
		1.41 V_{RHE}	1.4(5)		10(1)	2.68(2)	0.030
		1.43 V_{RHE}	1.4(5)		10(1)	2.69(2)	0.031
		1.46 V_{RHE}	1.3(5)		9(1)	2.69(2)	0.023
		1.48 V_{RHE}	1.0(6)		10(1)	2.70(3)	0.035
		1.51 V_{RHE}	0.9(5)		10(1)	2.70(3)	0.031
		1.53 V_{RHE}	0.9(5)		10(1)	2.68(3)	0.027
		1.56 V_{RHE}	0.9(5)		10(1)	2.70(3)	0.029
$Ir_{50}In_{50}$	Ir–O	OCV	2.2(3)	0.006	11(3)	1.96(2)	0.039
		OCV (cycled)	6.3(3)		10(1)	2.00(1)	0.011
		1.16 V_{RHE}	6.2(4)		11(1)	2.00(1)	0.017
		1.26 V_{RHE}	6.1(4)		10(1)	1.99(1)	0.019
		1.31 V_{RHE}	6.3(3)		9(1)	1.98(1)	0.010
		1.38 V_{RHE}	6.4(3)		9(1)	1.97(1)	0.013
		1.41 V_{RHE}	6.4(3)		9(1)	1.97(1)	0.012
		1.43 V_{RHE}	6.6(4)		9(1)	1.97(1)	0.013
		1.46 V_{RHE}	6.6(4)		9(1)	1.96(1)	0.015
		1.48 V_{RHE}	6.7(4)		9(1)	1.97(1)	0.013
		1.56 V_{RHE}	6.8(8)		9(3)	1.96(2)	0.052
	Ir–M	OCV	5.7(6)	0.006	4(2)	2.66(1)	0.039
		OCV (cycled)	N/A	N/A	N/A	N/A	N/A
		1.16 V_{RHE}					

		1.26 V_{RHE}					
		1.31 V_{RHE}					
		1.38 V_{RHE}					
		1.41 V_{RHE}					
		1.43 V_{RHE}					
		1.46 V_{RHE}					
		1.48 V_{RHE}					
		1.56 V_{RHE}					

† For $Ir_{50}In_{50}$, the fitted results of the Ir–M shells show a high standard deviation which indicates the possible absence of Ir–M shells (here denoted as N/A).

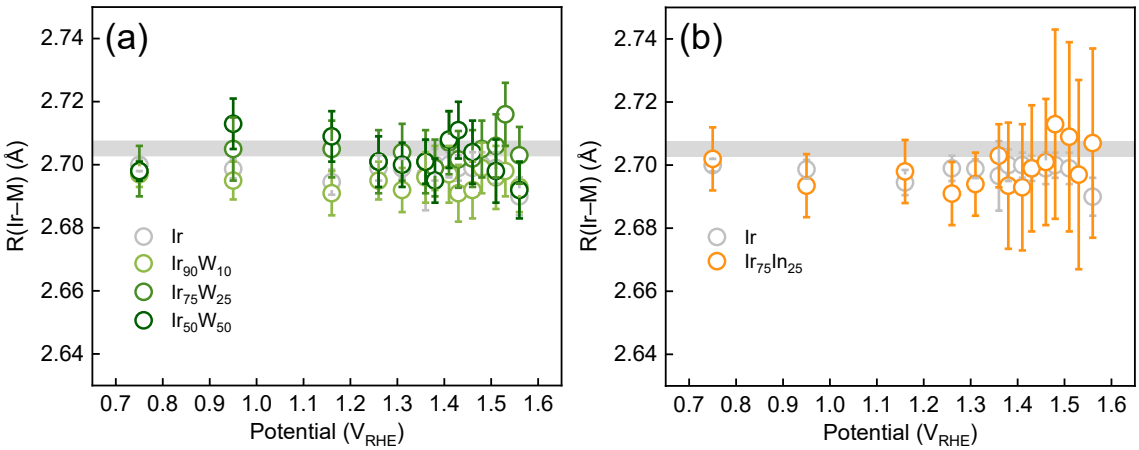

Figure S15. EXAFS derived interatomic distances of monometallic Ir and (a) Ir-W or (b) Ir-In as a function of the applied potential. Grey area indicates the fitted Ir–Ir interatomic distance (*i.e.*, 2.706(3) Å) of the Ir reference (Sigma-Aldrich).

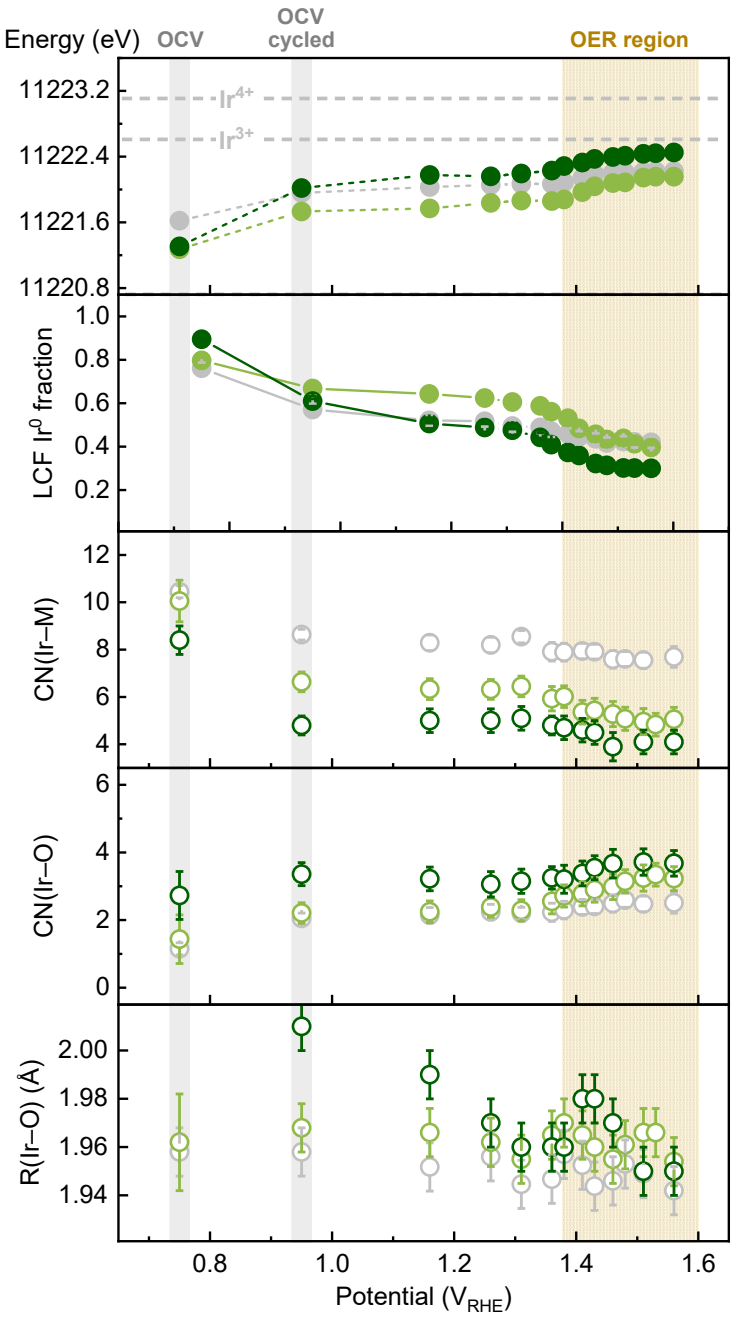

Figure S16. Ir L_3-edge WL peak positions, LCF-derived Ir^0 fractions, fitted Ir–M and Ir–O coordination numbers, fitted Ir–O interatomic distances for $Ir_{90}W_{10}$ and $Ir_{50}W_{50}$ as a function of potential in 0.1 M $HClO_4$. The baseline of the first panel indicates the peak position of the fitted metallic Ir reference (11220.72 eV). All spectra were acquired in fluorescence mode, except for the Ir, $Ir(acac)_3$, and IrO_2 references. Loading: 2 $mg_{catalyst}$ cm^{-2} (on carbon paper).

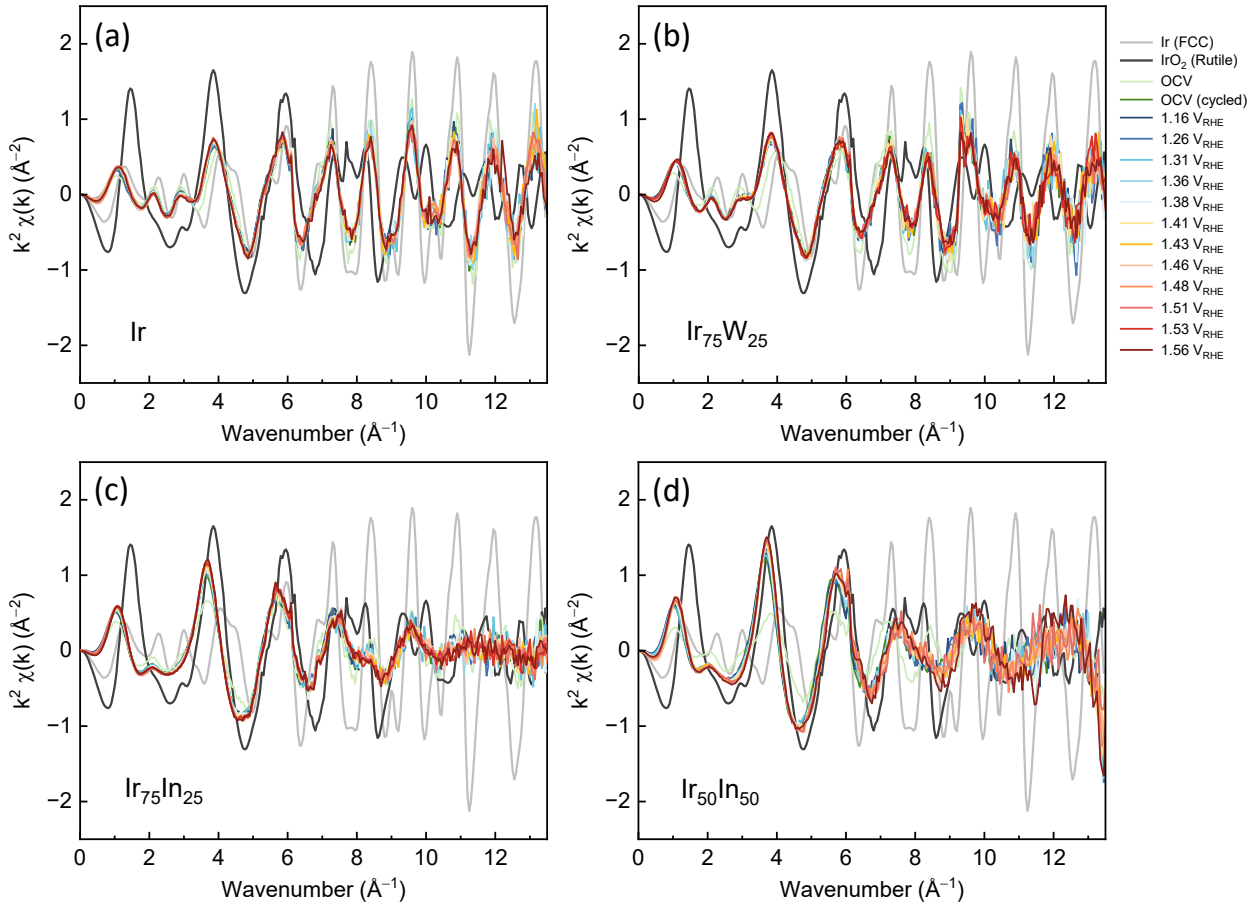

Figure S17. k^2-weighted Ir L_3-edge EXAFS data in k-space of (a) Ir, (b) $Ir_{75}W_{25}$, (c) $Ir_{75}In_{25}$, and (d) $Ir_{50}In_{50}$ compared to that of the reference materials.

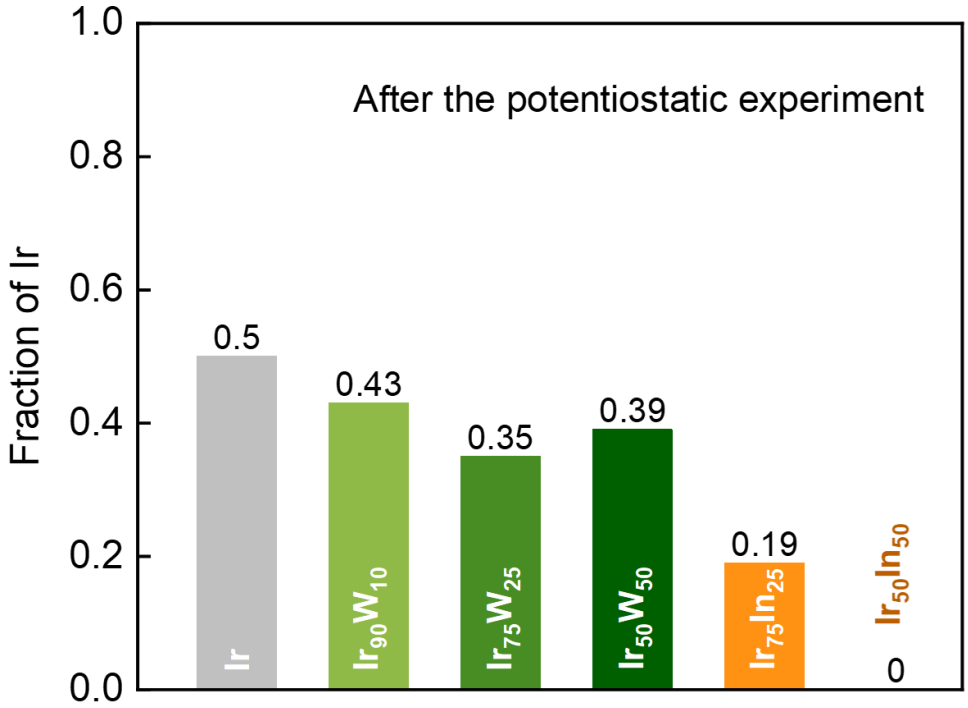

Figure S18. Fraction of metallic Ir in the Ir-M catalysts after potentiostatic experiments as determined by LCF.

Table S3. Comparison of TOF (unit: s^{-1}) of Ir, $Ir_{75}W_{25}$, and $Ir_{75}In_{25}$ and representative Ir-based electrocatalysts found in the literature (see also **Figure 5b**). The listed $TOF_{surface}$ are based on (1) Brunauer-Emmett-Teller (BET) surface area (if provided in the literature) of the electrocatalysts or (2) the reported particle size, Ir content, and catalyst loading for the nanoparticles (following the calculation method described in the Experimental section), unless mentioned otherwise.

Material	Overpotential (mV)	$TOF_{surface}$	TOF_{IrOx}	TOF_{bulk}	Reference
Ir	270	0.7	0.18	0.09	This work
$Ir_{75}W_{25}$		1.46	0.34	0.22	
$Ir_{75}In_{25}$		0.81	0.20	0.17	
1T-IrO_2 (2D-material)		3.00	N/A	0.15	[27]
$SrCo_{0.9}Ir_{0.1}O_{3-\delta}$		2.5[a]		0.03	[15]
Ir	300	1.63	0.57	0.29	This work
$Ir_{75}W_{25}$		3.76	1.05	0.68	
$Ir_{75}In_{25}$		1.82	0.60	0.48	
Mass-selected $Ir_{0.1}Ta_{0.9}O_{2.45}$		1.5±0.8[b]	N/A	0.36	[3]
$Ir_{78}Rh_{22}$ (nanoparticles)		1.15[c]		0.50	[28]
$IrNiO_x$ (nanoparticles)		N/A		0.348	[19]
O-IrVMn/IrO_x (nanoparticles)		0.56		0.27	[29]
Amorphous Ir nanosheets		N/A		0.105	[30]
Li-IrO_x		0.31		0.0647	[31]
$W_{0.99}Ir_{0.01}O_{3-\delta}$		1.03[d]		0.013[d]	[32]
IrO_2 (plasma oxidized)		0.47		0.01	[32]
Ir-IrO_x/C (2D-material)		0.0953		N/A	[33]

[a] Based on the authors' assumption of a 10 nm reconstructed layer involved in the reaction.

[b] Active surface Ir atoms were estimated by ^{13}CO-stripping in an EC-MS setup.

[c] The TOF reported when normalized by the measured ECSA was *ca.* 5.2 s^{-1}. The $TOF_{surface}$ value re-calculated here are based on the reported particle size, Ir content, and catalyst loading.

[d] The $TOF_{surface}$ of $W_{0.99}Ir_{0.01}O_{3-\delta}$ was calculated using the number of metal atoms on the catalyst surface, whereas TOF_{bulk} was based on all Ir atoms in the catalyst.

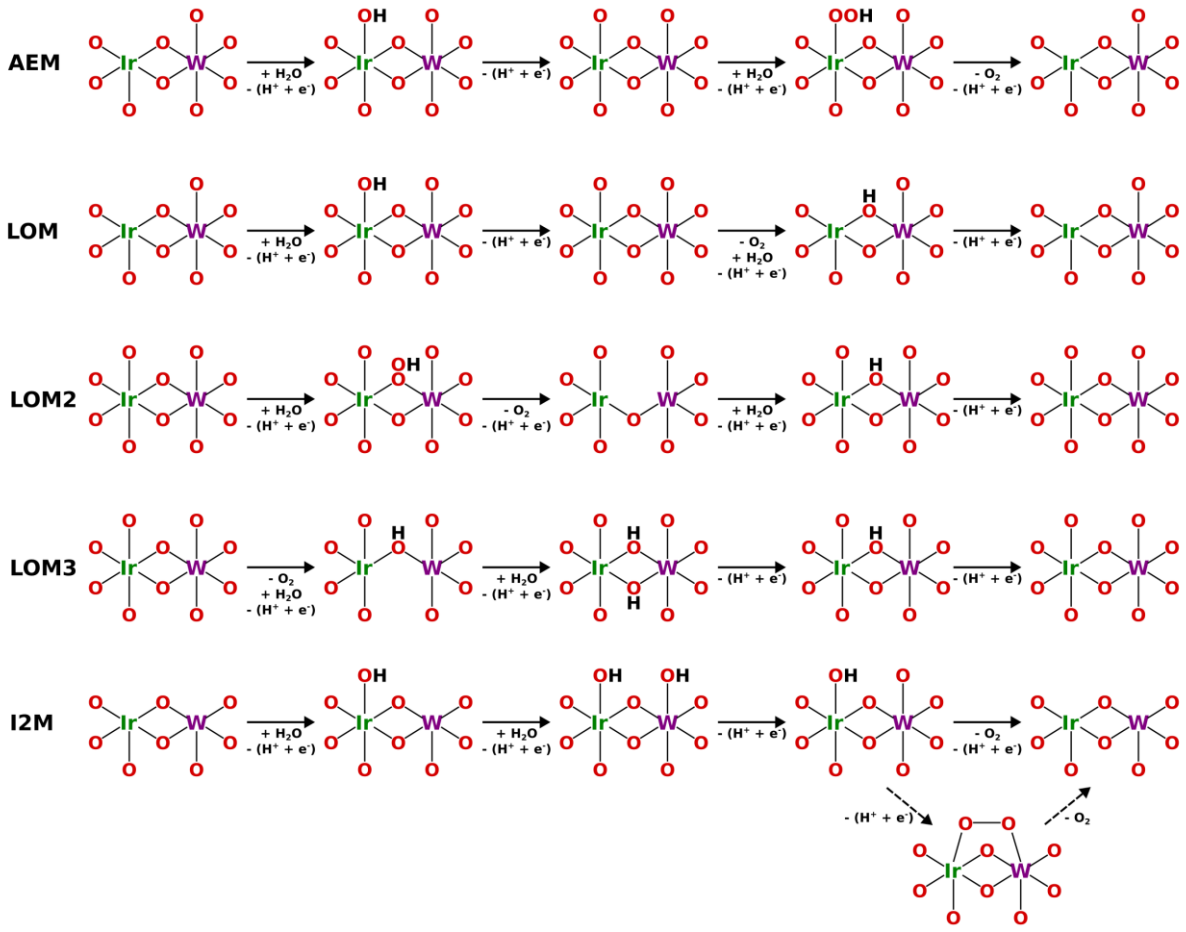

Figure S19. Various OER mechanisms considered for unsubstituted and W-substituted IrO_2 (110). The reaction intermediates for pathways LOM2 and LOM3 were identified as unstable, no potential energy minimum was found.

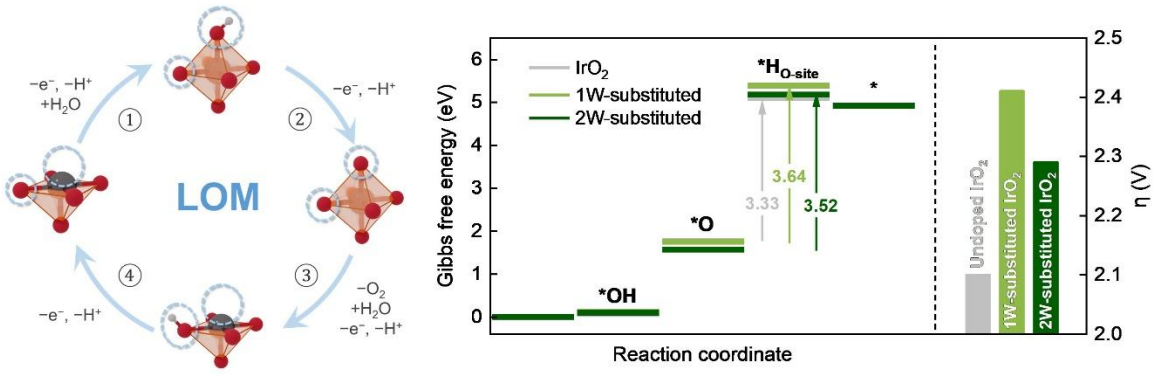

Figure S20. The proposed LOM reaction mechanism and the calculated free energy diagram and OER overpotentials for unsubstituted and W-substituted IrO_2 (110).

Table S4. Comparison of DFT-computed reaction free energies and OER overpotentials via AEM, LOM and I2M pathways for unsubstituted and W/In-substituted IrO_2 (110).

	ΔG_1 (eV)	ΔG_2 (eV)	ΔG_3 (eV)	ΔG_4 (eV)	η_{OER} (V)
			AEM		
Unsubstituted	0.07	1.70	1.19	**1.96**	0.73
1W-substituted	0.12	1.63	1.37	**1.80**	0.57
2W- substituted	0.10	1.56	1.46	**1.79**	0.56
1In- substituted	0.68	**2.90**	-0.66	2.00	1.67
2In- substituted	spontaneous formation of $*O_{cus}$-$*O_{cus}$ dimer				
			LOM		
Unsubstituted	0.07	1.70	**3.33**	−0.19	2.10
1W-substituted	0.12	1.63	**3.64**	−0.47	2.41
2W- substituted	0.10	1.56	**3.52**	−0.26	2.29
			I2M		
Unsubstituted	−0.04	0.03	1.72	**3.21**	1.98
1W-substituted	−0.13	−0.57	0.76	**4.87**	3.64
2W- substituted	−0.06	−0.60	0.69	**4.90**	3.67

The reaction intermediates for pathways LOM2 and LOM3 (**Figure S19**) were identified as unstable, no potential energy minimum was found.

For all three models (unsubstituted IrO_2, 1W-substituted, 2W-substituted, see **Figure 6a** in the main text), the AEM pathway is associated with the lowest overpotentials.

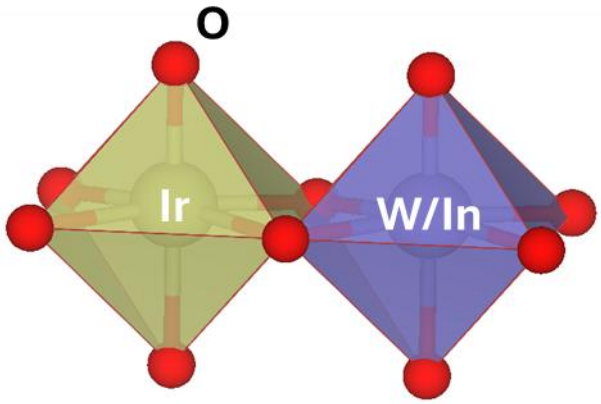

Figure S21. Schematics showing atoms for which the Bader charges were calculated (**Table S5**).

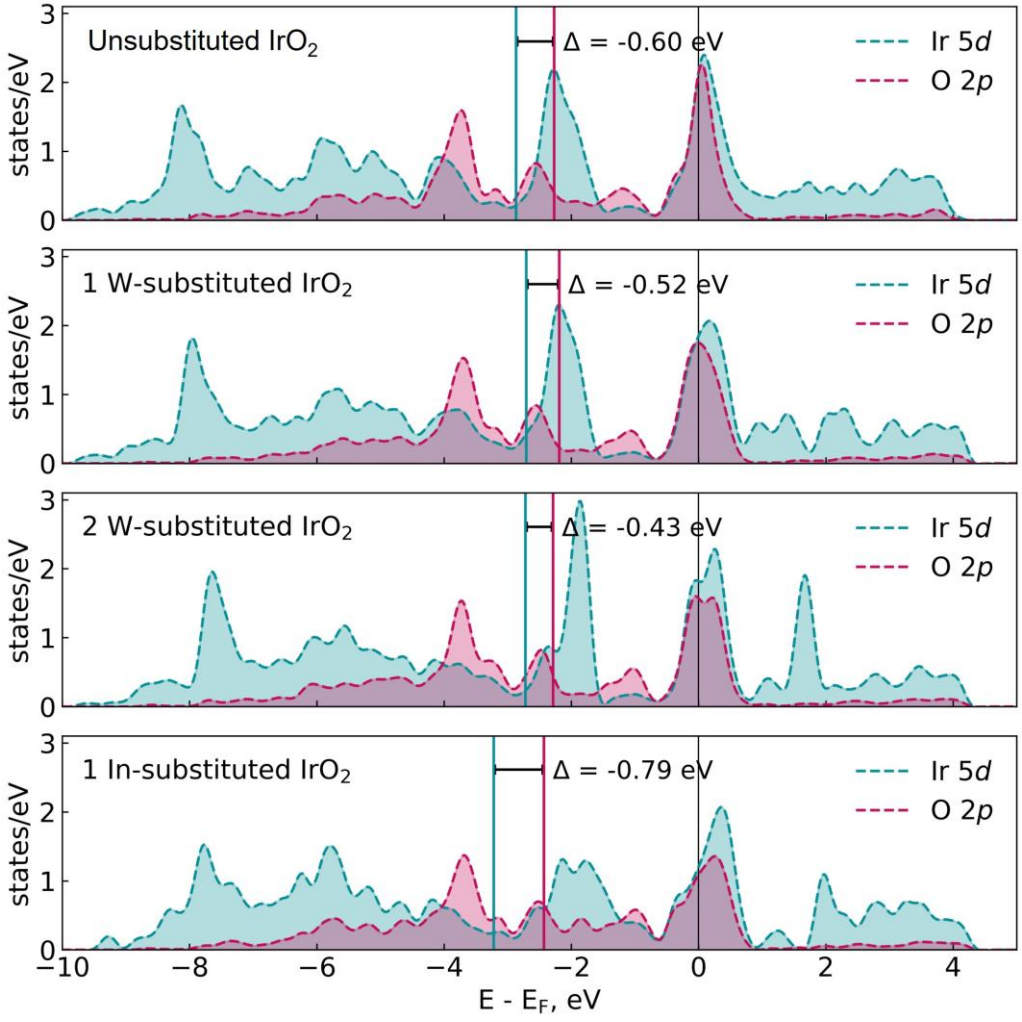

Figure S22. Projected density of states (PDOS) of Ir 5*d* and O 2*p* in unsubstituted, 1 W-substituted, 2 W-substituted and 1 In-substituted IrO_2.

Table S5. Bader charges of O, Ir, W and In and the Ir *5d*–O *2p* band-center difference of the different catalyst models examined.

		Bader charges (eV)			Band center difference
	ΔG_O	O	Ir	W or In	Ir *5d*–O *2p*
Undoped	1.77	−0.48	1.88	N/A	−0.60
1W-substituted	1.75	−0.49	1.82	2.71	−0.52
2W-substituted	1.66	−0.49	1.83	2.67	−0.43
1In-substituted	3.58	−0.47	1.88	1.81	−0.79
2In-substituted	spontaneous formation of $*O_{cus}$-$*O_{cus}$ dimer				

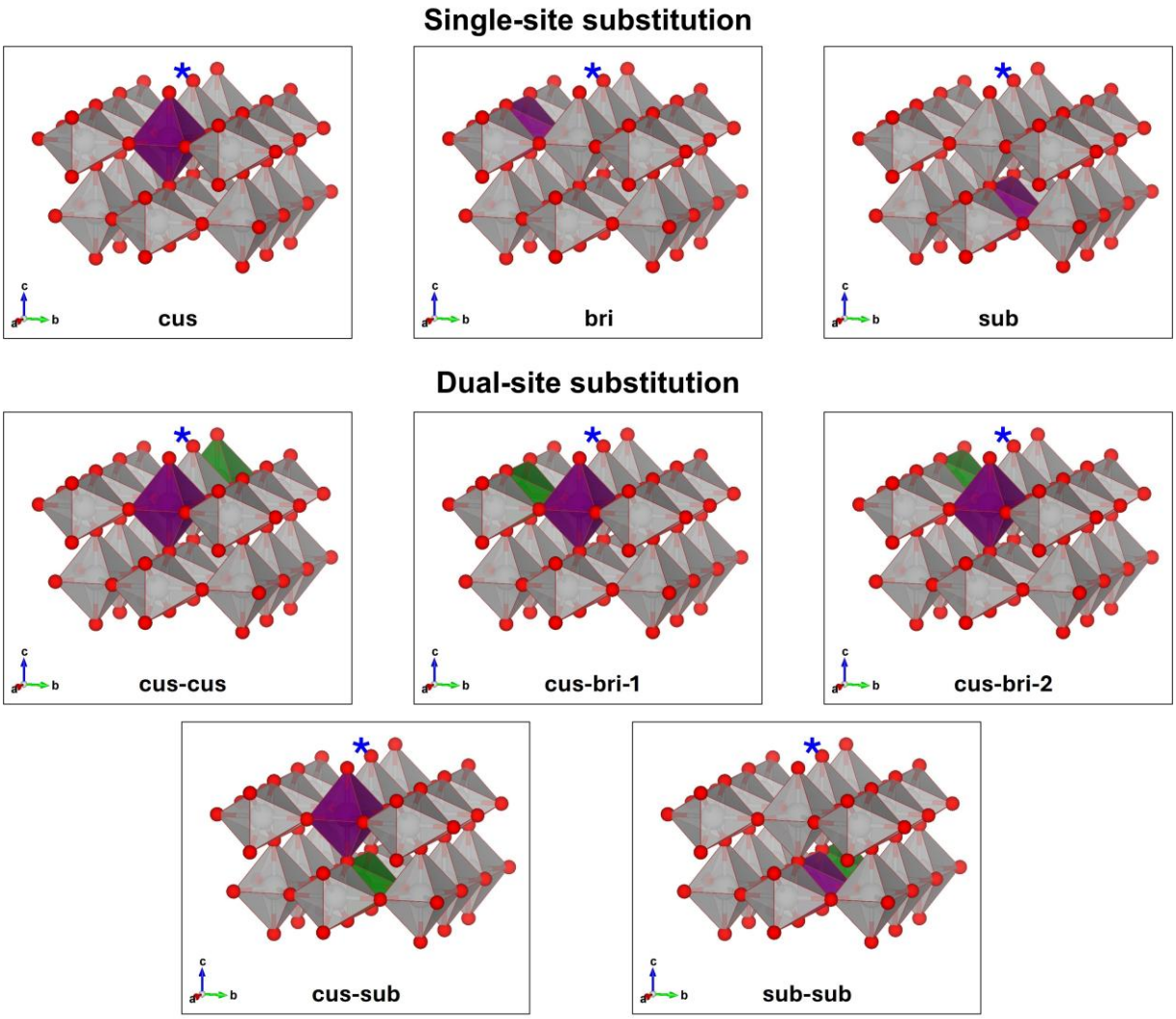

Figure S23. Screening of a series of possible configurations of 1W- and 2W-substituted IrO_2 models ("sub" stands for subsurface).

Table S6. Comparison of DFT-calculated reaction free energies and corresponding OER overpotentials via the AEM pathway for different 1W- and 2W-substituted IrO_2 (110) models.

AEM	ΔG_1 (eV)	ΔG_2 (eV)	ΔG_3 (eV)	ΔG_4 (eV)	η_{OER} (V)
Unsubstituted IrO_2	0.07	1.70	1.19	1.96	**0.73**
1 W-substituted IrO_2, cus	0.12	1.63	1.37	1.80	**0.57**
1 W-substituted IrO_2, bri	0.02	1.69	1.26	1.95	**0.72**
1 W-substituted IrO_2, sub	0.18	1.54	1.28	1.92	**0.69**
2 W-substituted IrO_2, cus-cus	0.10	1.56	1.46	1.79	**0.56**
2 W-substituted IrO_2, cus-bri-1	0.05	1.63	1.39	1.85	**0.62**
2 W-substituted IrO_2, cus-bri-2	0.07	1.65	1.38	1.82	**0.59**
2 W-substituted IrO_2, cus-sub	0.15	1.58	1.45	1.75	**0.52**
2 W-substituted IrO_2, sub-sub	0.37	1.54	1.28	1.73	**0.50**

The OER steps associated with the respective ΔG values are presented in **Figure S19**.

References

1. L. Fu, P. Cai, G. Cheng and W. Luo, *Sustainable Energy Fuels*, 2017, **1**, 1199-1203.
2. M. D. Obradović, B. D. Balanč, U. Č. Lačnjevac and S. L. Gojković, *J. Electroanal. Chem.*, 2021, **881**.
3. Y.-R. Zheng, J. Vernieres, Z. Wang, K. Zhang, D. Hochfilzer, K. Krempl, T.-W. Liao, F. Presel, T. Altantzis, J. Fatermans, S. B. Scott, N. M. Secher, C. Moon, P. Liu, S. Bals, S. Van Aert, A. Cao, M. Anand, J. K. Nørskov, J. Kibsgaard and I. Chorkendorff, *Nat. Energy*, 2021, **7**, 55-64.
4. H. Du, *Ultramicroscopy*, 2015, **151**, 62-67.
5. J. Shanmugam, K. B. Borisenko, Y.-J. Chou and A. I. Kirkland, *SoftwareX*, 2017, **6**, 185-192.
6. B. Ravel and M. Newville, *J. Synchrotron Radiat.*, 2005, **12**, 537-541.
7. G. Kresse and J. Furthmüller, *Phys. Rev. B*, 1996, **54**, 11169.
8. G. Kresse and J. Furthmüller, *Comput. Mater. Sci.*, 1996, **6**, 15-50.
9. G. Kresse and D. Joubert, *Phys. Rev. B*, 1999, **59**, 1758.
10. J. P. Perdew, K. Burke and M. Ernzerhof, *Phys. Rev. Lett.*, 1996, **77**, 3865.
11. Y. Lee, J. Suntivich, K. J. May, E. E. Perry and Y. Shao-Horn, *J. Phys. Chem. Lett.*, 2012, **3**, 399-404.
12. L. Yang, G. Yu, X. Ai, W. Yan, H. Duan, W. Chen, X. Li, T. Wang, C. Zhang, X. Huang, J. S. Chen and X. Zou, *Nat. Commun.*, 2018, **9**, 5236.

13. T. Kwon, H. Hwang, Y. J. Sa, J. Park, H. Baik, S. H. Joo and K. Lee, *Adv. Funct. Mater.*, 2017, **27**.
14. O. Diaz-Morales, S. Raaijman, R. Kortlever, P. J. Kooyman, T. Wezendonk, J. Gascon, W. T. Fu and M. T. Koper, *Nat. Commun.*, 2016, **7**, 12363.
15. Y. Chen, H. Li, J. Wang, Y. Du, S. Xi, Y. Sun, M. Sherburne, J. W. Ager, 3rd, A. C. Fisher and Z. J. Xu, *Nat. Commun.*, 2019, **10**, 572.
16. A. Grimaud, A. Demortière, M. Saubanère, W. Dachraoui, M. Duchamp, M.-L. Doublet and J.-M. Tarascon, *Nat. Energy*, 2016, **2**.
17. J. Feng, F. Lv, W. Zhang, P. Li, K. Wang, C. Yang, B. Wang, Y. Yang, J. Zhou, F. Lin, G. C. Wang and S. Guo, *Adv. Mater.*, 2017, **29**.
18. J. Xu, H. Jin, T. Lu, J. Li, Y. Liu, K. Davey, Y. Zheng and S.-Z. Qiao, *Sci. Adv.*, 2023, **9**, eadh1718.
19. H. N. Nong, T. Reier, H.-S. Oh, M. Gliech, P. Paciok, T. H. T. Vu, D. Teschner, M. Heggen, V. Petkov, R. Schlögl, T. Jones and P. Strasser, *Nat. Catal.*, 2018, **1**, 841-851.
20. J. Park, Y. J. Sa, H. Baik, T. Kwon, S. H. Joo and K. Lee, *ACS Nano*, 2017, **11**, 5500-5509.
21. S. B. Scott, J. Kibsgaard, P. C. K. Vesborg and I. Chorkendorff, *Electrochim. Acta*, 2021, **374**.
22. S. B. Scott, J. E. Sorensen, R. R. Rao, C. Moon, J. Kibsgaard, Y. Shao-Horn and I. Chorkendorff, *Energy Environ. Sci.*, 2022, **15**, 1988-2001.
23. F. Y. Xie, L. Gong, X. Liu, Y. T. Tao, W. H. Zhang, S. H. Chen, H. Meng and J. Chen, *J. Electron Spectros. Relat. Phenomena*, 2012, **185**, 112-118.
24. T. Pauporte´, Y. Soldo-Olivier and R. Faure, *J. Phys. Chem. B*, 2003, **107**, 8861-8867.
25. X. Carrier, E. Marceau, H. Carabineiro, V. Rodríguez-González and M. Che, *Phys. Chem. Chem. Phys.*, 2009, **11**, 7527-7539.
26. M. Juelsholt, O. Aalling-Frederiksen, T. Lindahl Christiansen, E. T. Kjær, N. Lefeld, A. Kirsch and K. M. Jensen, *Inorg. Chem.*, 2023, **62**, 14949-14958.
27. Q. Dang, H. Lin, Z. Fan, L. Ma, Q. Shao, Y. Ji, F. Zheng, S. Geng, S. Z. Yang, N. Kong, W. Zhu, Y. Li, F. Liao, X. Huang and M. Shao, *Nat. Commun.*, 2021, **12**, 6007.
28. H. Guo, Z. Fang, H. Li, D. Fernandez, G. Henkelman, S. M. Humphrey and G. Yu, *ACS Nano*, 2019, **13**, 13225-13234.
29. H. Luo, F. Lin, Q. Zhang, D. Wang, K. Wang, L. Gu, M. Luo, F. Lv and S. Guo, *J. Am. Chem. Soc.*, 2024, **146**, 19327-19336.
30. G. Wu, X. Zheng, P. Cui, H. Jiang, X. Wang, Y. Qu, W. Chen, Y. Lin, H. Li, X. Han, Y. Hu, P. Liu, Q. Zhang, J. Ge, Y. Yao, R. Sun, Y. Wu, L. Gu, X. Hong and Y. Li, *Nat. Commun.*, 2019, **10**, 4855.
31. J. Gao, C. Q. Xu, S. F. Hung, W. Liu, W. Cai, Z. Zeng, C. Jia, H. M. Chen, H. Xiao, J. Li, Y. Huang and B. Liu, *J. Am. Chem. Soc.*, 2019, **141**, 3014-3023.
32. S. Kumari, B. P. Ajayi, B. Kumar, J. B. Jasinski, M. K. Sunkara and J. M. Spurgeon, *Energy Environ. Sci.*, 2017, **10**, 2432-2440.
33. L. Zu, X. Qian, S. Zhao, Q. Liang, Y. E. Chen, M. Liu, B. J. Su, K. H. Wu, L. Qu, L. Duan, H. Zhan, J. Y. Zhang, C. Li, W. Li, J. Y. Juang, J. Zhu, D. Li, A. Yu and D. Zhao, *J. Am. Chem. Soc.*, 2022, **144**, 2208-2217.